# Screening properties and plasmons of Hg(Cd)Te quantum wells

Stefan Juergens,[1] Paolo Michetti,[2] and Björn Trauzettel[1]

[1]*Institute of Theoretical Physics and Astrophysics, University of Würzburg, D-97074 Würzburg, Germany*
[2]*Institute of Theoretical Physics, TU Dresden, D-01062 Dresden, Germany*

Under certain conditions, Hg(Cd)Te quantum wells (QWs) are known to realize a time-reversal symmetric, two-dimensional topological insulator phase. Its low-energy excitations are well described by the phenomenological Bernevig-Hughes-Zhang (BHZ) model that interpolates between Schrödinger and Dirac fermion physics. We study the polarization function of this model in the random phase approximation (RPA) in the intrinsic limit and at finite doping. While the polarization properties in RPA of Dirac and Schrödinger particles are two comprehensively studied problems, our analysis of the BHZ model bridges the gap between these two limits, shedding light on systems with intermediate properties. We gain insight into the screening properties of the system and on its characteristic plasma oscillations. Interestingly, we discover two different kinds of plasmons that are related to the presence of intra- and interband excitations. Observable signatures of these plasmons are carefully analyzed in a variety of distinct parameter regimes, including the experimentally relevant ones for Hg(Cd)Te QWs. We conclude that the discovered plasmons are observable by Raman or electron-loss spectroscopy.

## I. INTRODUCTION

Topological insulators (TIs) are among the most actively investigated systems in condensed matter physics [1–3]. In reality, there is evidence for their existence in two [4] and three [5] spatial dimensions. Due to bulk-boundary correspondence, nontrivial topological states of matter have edge states at their boundaries with peculiar transport and optical properties. For instance, the two-dimensional (2D), time-reversal symmetric quantum spin Hall state—that is realized in Hg(Cd)Te quantum wells (QWs)—is known to come along with helical edge states that are protected against elastic backscattering of nonmagnetic impurities [6,7]. However, not only the edge-state physics of these systems is interesting but also the 2D bulk physics bears exciting novelties. The low-energy excitations of Hg(Cd)Te QWs are described by a model—the Bernevig-Hughes-Zhang (BHZ) model [8]—that interpolates between the limiting cases of Schrödinger and Dirac fermions. This interplay between Schrödinger and Dirac physics constitutes an opportunity for new phenomena to emerge. We have, for instance, recently discovered collective charge excitations at zero doping, i.e., intrinsic plasmons, in this system which are absent in both separate limits [9].

In this article, we complement our study of the screening properties and the collective charge excitations of Hg(Cd)Te QWs on the basis of the random phase approximation (RPA), and hence present a comprehensive analysis of its polarization function in the static and full dynamic limit, at zero and finite doping. Continuously tuning the parameters of the BHZ model, we reproduce the limits of pure Dirac and pure Schrödinger fermions and explore intermediate regimes, in order to understand how analogies and differences emerge. We support our numerical calculations of the polarization functions with analytical expressions derived by $f$-sum rules. In the static limit, we calculate the screening properties due to the intrinsic system and at finite doping, analyzing the induced charge density (with Friedel oscillations) in response to a charged impurity. Different from the Dirac fermion system graphene, where static screening in the intrinsic limit is momentum independent and can therefore be absorbed into an effective dielectric

constant [10,11], the BHZ model shows a significant momentum dependence that translates into a finite extent of the induced charge density. In the dynamic limit, we are particularly interested in a better understanding of the plasmon excitations of this system away from zero doping where we previously found a new plasmon due to the interplay between Schrödinger and Dirac fermion physics [9]. At finite doping, under certain conditions specified below that are, e.g., applicable to Hg(Cd)Te QWs, we find a coexistence between this novel (interband) plasmon and an ordinary (intraband) plasmon. Both plasmons can be rather weakly damped by single-particle excitations and should therefore be observable. Interestingly, the two plasmons respond to the topology of the band structure with a distinctive behavior. They seem to merge one into the other in a normal insulating phase, while they remain clearly resolved when the system realizes a topological insulator.

Generally, RPA is known to provide reliable predictions at large densities and in systems with a large number of fermionic degrees of freedom. While its validity was indeed questioned for the intrinsic Dirac limit, where the system is unable to screen the Coulomb interaction and strong renormalization effects are expected [12], RPA has been shown to yield a quantitative description of many-body effects in graphene [13,14]. It has been widely used for the study of plasmons in the Dirac model, including various forms of (multilayer) graphene and TI surface states; see Ref. [15] for a comprehensive review. Closely related to our work, the intraband plasmons of black phosphorous have been studied on the basis of RPA and an extended version of the BHZ model including anisotropy [16]. A similar study has been done for MoS$_2$ [17].

Our article is organized as follows. In Sec. II, we introduce the BHZ model and present the general formalism we employ to calculate the static and dynamical dielectric function and the induced charge density. The nature of the nontrivial pseudospin, the origin of possible interband plasmons, experimentally relevant parameters, and the different contributions to the $f$-sum rule are also discussed here. Subsequently, in Sec. III, we present the static screening properties, the dynamical excitation spectrum (new interband plasmon), and

the $f$-sum rule in the undoped regime. Here we revisit and go beyond the results from Ref. [9]. In Sec. IV, this analysis is extended to the case of finite doping where inter- and intraband excitations equally matter. We begin by discussing the ability of the BHZ model to interpolate between Dirac and Schrödinger physics. Afterwards, we have a closer look at parameters which are experimentally relevant for Hg(Cd)Te QWs; see Sec. IV E. In this limit, we find a coexistence of inter- and intraband plasmons occurring for energies and momenta which are suitable for Raman or electron-loss spectroscopy. We close this section by investigating the influence of a nontrivial topology on the plasmonic excitation spectrum. Finally, in Sec. V, a conclusion and a brief outlook are given.

## II. MODEL AND FORMALISM

The BHZ Hamiltonian [8] for a two-dimensional electron gas (2DEG) near the $\Gamma$ point has the form

$$
\begin{aligned}
H &= \begin{pmatrix} h\left(\boldsymbol{k}\right) & 0 \\ 0 & h^*\left(-\boldsymbol{k}\right) \end{pmatrix}, \\
h\left(\boldsymbol{k}\right) &= V(k) + \boldsymbol{d_k} \cdot \vec{\sigma}, \\
\boldsymbol{d_k} &= (Ak_x, \quad Ak_y, \quad M(k)).
\end{aligned}
\tag{1}
$$

Here $\vec{\sigma}$ are the Pauli matrices associated with the band-pseudospin degree of freedom [band $E_1$ and $H_1$ in Hg(Cd)Te quantum wells (QWs)], $V(k) = C - Dk^2$, $M(k) = M - Bk^2$ with $B, D < 0$. The system possesses time-reversal symmetry and $H$ is block diagonal in the Kramer's partner or spin degree of freedom. Restricting ourselves to the block $h(\boldsymbol{k})$, the results can be extended to the other one by applying the time-reversal operator. $h(\boldsymbol{k})$ describes fermions with intermediate properties between a Dirac and a conventional 2DEG system. The off-diagonal term ($A$ parameter) is typical for a Dirac system ($A \cong \hbar v_f$ in graphene), with $M$ the Dirac mass (corresponding to a gap of $2|M|$). We consider positive and negative masses, where the latter corresponds to an inversion of the band structure and the system is topologically nontrivial [8]. For simplicity, we restrict ourselves to a band structure with a minimum at the $\Gamma$ point, which limits the mass to $M > -\frac{1}{2}\frac{A^2}{|B|}$. In analogy to a 2DEG, the diagonal elements bear kinetic energy elements which preserve ($B$ parameter) and break ($D$ parameter) particle-hole (p-h) symmetry ($-B \mp D \cong \frac{1}{2m}$ for Schrödinger fermions with $m$ the quasiparticle mass).

The eigenstates of Eq. (1) are described by the following dispersion and pseudospin

$$
E_{k,\lambda} = V(k) + \lambda |\boldsymbol{d_k}|, \tag{2}
$$

$$
\lambda \hat{\boldsymbol{d}}_{\boldsymbol{k}} = \langle \boldsymbol{k}, \lambda | \vec{\sigma} | \boldsymbol{k}, \lambda \rangle \tag{3}
$$

with $\lambda = \pm$ for conduction and valence band. Note that we consider electrons to be perfectly localized on the 2D $X$-$Y$ plane and therefore we neglect the real shapes of the envelope functions due to the quantum confinement along the $Z$ direction [18].

### A. Energy and momentum scales

The BHZ model is characterized by intrinsic scales for momentum, $q_0 = \frac{A}{|B|}$, and energy, $E_0 = Aq_0$, which reflect

the interpolating character of the model between Dirac ($A$ parameter) and Schrödinger ($B$ parameter) system. Fermi momentum $k_f$ and chemical potential $\mu$ provide externally tunable momentum and energy scales, which we call Fermi scales in the following. We expect the ratio between Fermi and intrinsic scales to govern the physics of this system. We therefore define the dimensionless quantities

$$
\begin{aligned}
X &= \frac{q}{q_0}, \quad \Omega = \frac{\omega}{E_0}, \quad X_f = \frac{k_f}{q_0}, \\
\Omega_f &= \frac{\mu}{E_0}, \quad \xi_M = \frac{M}{E_0}, \quad \xi_D = \frac{D}{|B|},
\end{aligned}
\tag{4}
$$

where we set $\hbar = 1$ in the following. $\Omega_f$ is defined to be the energy to the wave vector $X_f$, such that $\Omega_f = \pm|\xi_M|$ if $X_f = 0$. For $X \sim 1$, we therefore expect intermediate physics, while in the limit $X, \Omega \to 0$ ($X, \Omega \to \infty$) the Dirac (2DEG) physics should be recovered.

### B. Polarization function

The linear response of a homogeneous system to an external applied potential is described by the density-density generalized susceptibility or retarded polarization function $\Pi^R(\boldsymbol{q}, \omega)$. This response comprises two main phenomena: screening, described by the real part $\text{Re}[\Pi^R(\boldsymbol{q}, \omega)]$, and dissipation by single-particle excitations (SPEs), given by the imaginary part $\text{Im}[\Pi^R(\boldsymbol{q}, \omega)]$. For the BHZ model, the polarization function in RPA yields the expression

$$
\Pi^R(X, \Omega) = \frac{g_s}{|B|} \sum_{\lambda, \lambda'} \int \frac{d^2\tilde{X}}{4\pi^2} \mathcal{F}_{\tilde{X}, \tilde{X}'}^{\lambda, \lambda'} \frac{f(\epsilon_{\tilde{X}, \lambda}) - f(\epsilon_{\tilde{X}', \lambda'})}{\Omega + i0^+ + \epsilon_{\tilde{X}, \lambda} - \epsilon_{\tilde{X}', \lambda'}},
\tag{5}
$$

with $\tilde{X}' = \tilde{X} + X$, $0^+$ a positive infinitesimal, $g_s = 2$ for spin degeneracy, $\epsilon_{\tilde{X}, \lambda} = E_{q_0 \tilde{X}, \lambda}/E_0 = -\xi_D X^2 + \lambda \sqrt{(\xi_M + X^2)^2 + X^2}$, and $f(\epsilon) = \frac{1}{e^{\bar{\beta}(\epsilon - \Omega_f)} + 1}$ the Fermi-Dirac function with $\bar{\beta} = \frac{E_0}{k_B T}$ and $k_B$ the Boltzmann constant. In the following we will assume zero temperature, $T = 0$. The overlap factor is given by

$$
\mathcal{F}_{X, X'}^{\lambda, \lambda'} = |\langle \boldsymbol{k}, \lambda | \boldsymbol{k}', \lambda' \rangle|^2 = \tfrac{1}{2}[1 + \lambda \lambda' \hat{\boldsymbol{d}}_{q_0 X} \cdot \hat{\boldsymbol{d}}_{q_0 X'}]. \tag{6}
$$

Equation (5) implies that $|B|\Pi^R(X, \Omega)$ is only a function of the reduced dimensionless variables $X$ and $\Omega$ and parametrically depends on $\xi_M$, $\xi_D$, and $X_f$.

### C. Overlap factor

In the massless Dirac limit ($B = M = 0$), eigenspinors are characterized by their helicity and consequently the overlap factor $\mathcal{F}_{\boldsymbol{k}, \boldsymbol{k}'}^{\lambda, \lambda'} = \frac{1}{2}(1 + \lambda \lambda' \cos \theta)$ only depends on the angle $\theta$ between $\boldsymbol{k}$ and $\boldsymbol{k}'$. It is strictly 1 (zero) for states with the same (opposite) helicity.

In the BHZ model, the quadratic terms have the effect of turning the pseudospin of the eigenstates out of plane in opposite directions for conduction and valence bands at large $X$; see Fig. 1. This results in a decay of the overlap factor down to 0 in the limit of a conventional 2DEG system ($A \to 0$ or $X \to \infty$).
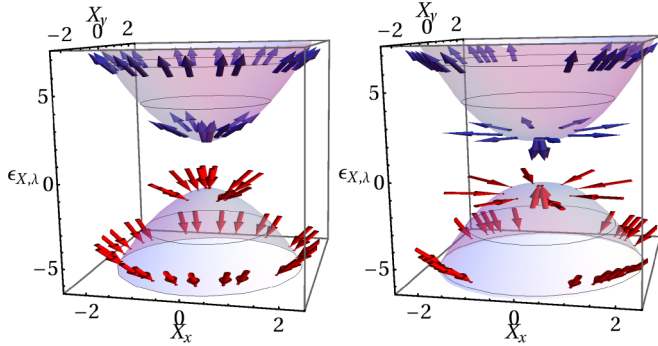
FIG. 1. (Color online) Dispersion relation and pseudospin of a NI (a), $\xi_M = \frac{4}{9}$, and a TI phase (b), $\xi_M = -\frac{4}{9}$. The bands are separated by an additional $2\epsilon_{X,\lambda}$ for better illustration of the pseudospin.

A finite mass $\xi_M \neq 0$ has a similar effect, but in the limit of $X \leqslant |\xi_M|$. The pseudospin turns in the same (opposite) direction as for the quadratic term for positive (negative) mass; see Fig. 1. This has the direct consequence that for a normal insulator (NI) phase the interband overlap factor is reduced, while it is increased for a TI phase. On the contrary, a positive (negative) mass enhances (diminishes) the intraband overlap factor. This picture is also confirmed in Sec. II G by calculating the $f$-sum rule.

### D. Coulomb interaction

The bare Coulomb interaction $v(q) = \frac{e^2}{2\epsilon_0 q}$ in an electron gas is modified by screening into the effective interaction $v_{\text{eff}}(q,\omega) = \frac{v(q)}{\epsilon(q,\omega)}$. There, screening is described by the dynamical dielectric function. Employing dimensionless units, it acquires the form

$$\frac{\epsilon(X,\Omega)}{\epsilon_r} = 1 - \alpha g(X,\Omega), \tag{7}$$

where we have introduced the interaction strength parameter $\alpha$ (effective Dirac fine structure constant [19]) and the dimensionless function $g(X,\Omega)$:

$$\alpha = \frac{1}{A}\frac{e^2}{4\pi\epsilon_0\epsilon_r}, \tag{8}$$

$$g(X,\Omega) = 2\pi\frac{|B|}{X}\Pi^R(X,\Omega). \tag{9}$$

In graphene one finds [20] $\alpha = 2.2/\epsilon_r$, while in Hg(Cd)Te QWs it is of the order $\alpha \approx 4/\epsilon_r$ [21,22]. Here, $\epsilon_r$ is the background dielectric constant, accounting for screening of internal electronic shells, while $-\alpha g(X,\Omega)$ gives the dynamic screening due to electrons in the low-energy bands. Zeros of $\epsilon(X,\Omega)$ describe a density-density (longitudinal) perturbation of the system that it is able to sustain itself, which forms a collective mode called plasmon. It is defined by

$$\epsilon(X,\Omega_p - i\Gamma) = 0 \tag{10}$$

with the plasma frequency $\Omega_p$, and the finite imaginary part $\Gamma = \frac{\gamma}{E_0}$ accounts for the possible damping due to single-particle excitations [23].

The dissipation of the interacting system, including both single-particle excitation and the plasmon mode, is then described by the imaginary part of the interacting polarization function $\Pi^{RPA}(X,\Omega) = \frac{\Pi^R(X,\Omega)}{\epsilon(X,\Omega)}$. In order to compare to the noninteracting one, we will plot the normalized functions

$$\Pi_{rpa}^{Im} \equiv \epsilon_r \text{Im}[\Pi^{RPA}], \quad \Pi^{Im} \equiv \text{Im}[\Pi^R], \quad \Pi^{Re} \equiv \text{Re}[\Pi^R]$$

in the following, with $\epsilon_r \Pi^{RPA} \underset{\alpha\to 0}{=} \Pi^R$.

#### 1. (Anti)Screening and intrinsic plasmons

In RPA, Eq. (7) characterizes the screening of the interaction between two electrons exchanging momentum $X$ and energy $\Omega$, by the creation of electron-hole pairs in the electron gas with the same momentum $X$. If these pairs are resonant in energy $\Omega_{eh} = \Omega$, they correspond to a physical process leading to dissipation and a lowering of the Coulomb interaction—described by the imaginary part of the polarization function, Eq. (5). When $\Omega_{eh} \neq \Omega$, we have only virtual electron-hole pairs, which either still screen the interaction, if $\Pi^{Re} < 0$, or even enhance it (antiscreening effect), if $\Pi^{Re} > 0$. These effects depend on the energy of the created pair: for $\Omega_{eh} < \Omega$ one finds antiscreening, while $\Omega_{eh} > \Omega$ leads to a screening of the bare Coulomb interaction. This can be directly seen from the definition of the polarization function, Eq. (5). For every allowed excitation, the real part of the integrand in Eq. (5) becomes

$$\mathcal{F}_{\tilde{X},\tilde{X}'}^{1,\lambda}\frac{2\Omega_{eh}[\tilde{X},\tilde{X}']}{\Omega^2 - \Omega_{eh}[\tilde{X},\tilde{X}']^2}, \tag{11}$$

with $\lambda = 1$ ($\lambda = -1$) for intraband (interband) excitations. Therefore every process with energy less than $\Omega$ increases $\Pi^{Re}$, lowering $\epsilon$ and thus increasing the interaction.

In the intrinsic Dirac system within RPA one finds $\Pi^{Re} = 0$ for all energies $\Omega$ where electron-hole excitations are allowed [15]. Thus the screening effect of virtual excitations with $\Omega_{eh} > \Omega$ cancels exactly with the one from excitations with $\Omega_{eh} < \Omega$, such that the only screening comes from the resonant process $\Omega_{eh} = \Omega$. In the BHZ model, the high-energy excitations become less likely as the electron and the hole band get decoupled for large $\Omega$. Additionally their excitation energy is higher as in the Dirac case for the same momentum $X$, leading to an additional reduction of their influence on $\Pi^{Re}$ due to the Lorentzian in Eq. (11). Further, low-energy excitations become more important, as processes are allowed that were forbidden in the Dirac system by helicity (see Sec. IV D 3 for details). Combining these effects, one finds the virtual excitations which increase the Coulomb interaction, $\Omega_{eh} < \Omega$, dominating for larger frequency $\Omega$, leading to an increased effective interaction and the possibility of intrinsic plasmons in the BHZ model [9].

More mathematically speaking, the described effects alter the high-energy behavior of $\Pi^{Im}$ from a decay like $\Omega^{-1}$ in the Dirac case to a $\Omega^{-2}$ decay in the BHZ model, as is shown in Sec. III C. Taking the Kramers-Kronig relation $\Pi^{Re}(X,\Omega) = \frac{1}{\pi}\int_0^\infty d\Omega' \frac{2\Omega'}{\Omega'^2 - \Omega^2}\Pi^{Im}(X,\Omega')$ one finds directly that the real part of the polarization changes sign for $\Pi^{Im} \propto \Omega^{-2}$, but not for $\Pi^{Im} \propto \Omega^{-1}$. In more general terms, one can expect intrinsic interband plasmons to appear in all models for which $\Pi^{Im}$ decays faster as $\Omega^{-1}$ for high energies.

### E. Static limit and screening

The static limit of the polarization function is obtained by sending $\Omega \to 0$ at finite momentum $X$ in Eq. (5). In this limit we can easily analyze the response of the system to the application of a static (or sufficiently slowly varying) external potential. An important physical problem of this kind is the screening of a charged impurity by the electronic system.

The static polarization is a strictly real function, that we define as

$$\Pi(X) \equiv \Pi^R(X,0) = \Pi_0(X) + \Pi_\mu(X). \tag{12}$$

In a multiband system, like the BHZ model, it is useful to separate the contributions to the static polarization coming from the intrinsic neutral system, $\Pi_0(X)$ (obtained for $\mu = 0$), and the contribution due to a finite charge density, $\Pi_\mu(X)$ (finite $\mu$). Consistently with the notation of Eq. (12), the dielectric function, Eq. (7), can therefore be rearranged into

$$\epsilon(X) \equiv \epsilon(X,0) = \epsilon_r[1 - \alpha g_0(X) - \alpha g_\mu(X)]. \tag{13}$$

From the static dielectric constant we can find the induced charge density in response to a test charge $Ze$ placed at the origin. The variation of the electronic charge density in momentum space corresponds to $Zen(X)$, where $n(X)$ is given by [23]

$$n(X) = \frac{1}{\epsilon(X)} - 1 = \frac{1}{\epsilon_r[1 - \alpha g(X)]} - 1$$
$$= n_r(X) + n_0(X) + n_\mu(X). \tag{14}$$

Here the induced charge density can be seen as a sum of three contributions of different physical nature. The first is due to the background polarization $n_r(X)$ (high-energy polarization of the system), the second to the intrinsic polarization $n_0(X)$ (polarization of the neutral system), and the third to the polarization of the finite charge density in the system $n_\mu(X)$, with

$$n_r(X) = \frac{1}{\epsilon_r} - 1, \tag{15}$$

$$n_0(X) = \frac{1}{\epsilon_r} \frac{\alpha g_0(X)}{1 - \alpha g_0(X)}, \tag{16}$$

$$n_\mu(X) = \frac{1}{\epsilon_r} \frac{1}{1 - \alpha g_0(X)} \frac{\alpha g_\mu(X)}{1 - \alpha g(X)}. \tag{17}$$

In real space, the density fluctuation (using physical dimensional units) is given by

$$n(r) = \frac{1}{2\pi} \int dq\, q\, J_0(qr) n(q),$$

with $J_0$ the zeroth-order Bessel function.

### F. Experimental parameters

Including Coulomb interaction, we now have a 4-dimensional parameter space consisting of $\xi_M$, $\xi_D$, $X_f$, and $\alpha$. This parameter space will be explored systematically in the following. While the exploration of the different physical behaviors featured by the BHZ model in different regions of this parameter space has a clear theoretical significance, we want to stress that our discussion is also relevant for experiments. In particular, realistic parameters for Hg(Cd)Te

QW structures [21,22] are roughly $\xi_D \leqslant -0.5$, $q_0 \approx 0.4\,\frac{1}{\text{nm}}$, $E_0 \approx 140$ meV, and masses $M$ with absolute values up to several meV. The interaction strength is around $\alpha \approx 4/\varepsilon_r \approx 0.3$ with an average $\varepsilon_r = 15$ from the CdTe substrate ($\varepsilon_r = 10$) and HgTe ($\varepsilon_r = 20$). Considering the experimental acceptable damping rate for plasmons, we refer to experiments on the surface states of a 3D TI [24]. There, plasmons with a ratio of $\frac{\Gamma}{\Omega_p} = 0.5$ are perfectly resolvable.

### G. $f$-sum rule

The $f$-sum rule for the polarization function provides the total spectral weight of all excitations in the system. It is identical for the interacting and noninteracting system, as the interaction conserves the number of particles. Thus the sum rule is a powerful tool to check our numerics. Additionally, it offers a deeper insight concerning the shift of spectral weight between the inter and intra SPEs as well as the different plasmons in the system.

#### 1. Definition and calculation

The $f$-sum rule is defined by [25]

$$-\frac{2}{\pi} \int_0^\infty d\omega\, \omega \text{Im}[\Pi(\mathbf{q},\omega)] = g_s \langle 0|[[n_\mathbf{q}, H^0], n_\mathbf{q}^\dagger]|0\rangle \tag{18}$$

with the density operator $n_\mathbf{q}^\dagger = \sum_\mathbf{k} \Psi_{\mathbf{k}+\mathbf{q}}^\dagger \Psi_\mathbf{k}$ and the Hamiltonian $H^0 = \sum_\mathbf{k} \Psi_\mathbf{k}^\dagger h(\mathbf{k}) \Psi_\mathbf{k}$ with $h(\mathbf{k})$ as defined in Eq. (1). $\Psi_\mathbf{k}$ is a spinor associated with the band-pseudospin degree of freedom [bands $E_1$ and $H_1$ in Hg(Cd)Te QWs]. The spin degree of freedom enters via the degeneracy factor $g_s = 2$. For the calculation we follow the steps outlined in the Appendix of Ref. [26], where the $f$-sum rule for the Dirac model is obtained. For the BHZ model the computational steps are the same; therefore we only present important intermediate results and differences to the Dirac limit. The commutator in Eq. (18) is given by

$$[[n_\mathbf{q}, H^0], n_\mathbf{q}^\dagger] = \sum_\mathbf{k} \left( \Psi_\mathbf{k}^\dagger H_{\mathbf{k},\mathbf{q}}^0 \Psi_\mathbf{k} - \Psi_{\mathbf{k}+\mathbf{q}}^\dagger H_{\mathbf{k}+\mathbf{q},\mathbf{q}}^0 \Psi_{\mathbf{k}+\mathbf{q}} \right)$$
$$- 2q^2 \sum_\mathbf{k} \Psi_{\mathbf{k}+\mathbf{q}}^\dagger \left( D\sigma_0 + B\sigma_z \right) \Psi_{\mathbf{k}+\mathbf{q}}, \tag{19}$$

with $H_{\mathbf{k},\mathbf{q}}^0 = A\mathbf{q} \cdot \boldsymbol{\sigma} - D\mathbf{q}(2\mathbf{k} + \mathbf{q})\sigma_0 - B\mathbf{q}(2\mathbf{k} + \mathbf{q})\sigma_z$. A simple shift of the momentum sums in Eq. (19) would put the first line to zero, but this is not allowed. In the same way as in the Dirac system, the operators are unbounded and one has to work with a large momentum cutoff $\kappa$. While in the Dirac limit one finds simply $H_{\mathbf{k},\mathbf{q}}^0 = A\mathbf{q} \cdot \boldsymbol{\sigma}$ and the second line of Eq. (19) would be zero, now the latter gives rise to a contribution depending on the chemical potential, as one would expect for a 2DEG. The sums in Eq. (19) are then converted into integrals and solved in the limit of large $\kappa$. Care has to been taken when converting the momentum cutoff $\kappa$ into the frequency cutoff $\lambda$, such that both integrals cover the same phase space.

### 2. Formulas

For a pure Dirac system one finds the $f$-sum rule [26]

$$\int_0^\lambda d\omega\, \omega \mathrm{Im}\left[\Pi(q,\omega)\right] = -\frac{g_s q^2 \lambda}{16}, \qquad (20)$$

where the cutoff $\lambda$ is needed as the Dirac spectrum is unbounded. In a 2DEG system one finds

$$\int_0^\infty d\omega\, \omega \mathrm{Im}\left[\Pi(q,\omega)\right] = \frac{g_s}{4}(B \pm D)k_f^2 q^2 = -\frac{\pi N q^2}{2m} \qquad (21)$$

with $N = \frac{g_s}{4\pi}k_f^2$ the electron density and $\mathrm{Im}[\Pi(q,\omega)] \neq 0$ only over a finite range of $\omega$. Similar to a Dirac system, the BHZ spectrum is unbounded which complicates the evaluation of the sum rule and makes it necessary to introduce a high-energy cutoff $\Lambda = \frac{\lambda}{E_0}$. We find approximately for $\Lambda \gg 1$

$$\begin{aligned}
f\sum &\equiv -\int_0^\lambda d\Omega\, \Omega |B| \mathrm{Im}\left[\Pi(X,\Omega)\right] \\
&= \frac{g_s}{8}X^2 \left[ \ln\left(\frac{2\Lambda e^{-1-2\xi_M+2|\Omega_f|}}{1+2X_f^2(1+\gamma\xi_D)+2\xi_M+2|\Omega_f|}\right) \right. \\
&\quad + \frac{1-X^2+4\xi_M}{\Lambda} \\
&\quad \left. - \frac{2X^4+(1+4\xi_M)^2-4X^2(2+7\xi_M)}{4\Lambda^2} \right] \\
&\quad + O\left(\frac{\xi_D}{\Lambda^2}\right) + O\left(\frac{1}{\Lambda^3}\right),
\end{aligned} \qquad (22)$$

with $\gamma = \mathrm{sgn}[\Omega_f]$ and Euler's number $e$, so the leading order term diverges logarithmically with $\Lambda$. This is due to the fact that $\mathrm{Im}[\Pi(X,\Omega)]$ decays like $\Omega^{-2}$ for $\Omega \gg 1$, and not as $\Omega^{-1}$ as for a Dirac system. The sum rule is exact up to order $\Lambda^{-1}$ ($\Lambda^{-2}$) for finite (zero) $\xi_D$.

The $f$-sum rules for BHZ, Dirac and 2DEG models are always proportional to $q^2 \propto X^2$ in the leading order, but otherwise distinct from one another. Taking the limit $A \to 0$ in the BHZ result, Eq. (22), gives the 2DEG case, Eq. (21) [34].

### 3. Comparing different orders in cutoff $\Lambda$

We begin our discussion of Eq. (22) by comparing the contributions from the different orders $O(\ln(\Lambda))$, $O(\Lambda^{-1})$, and $O(\Lambda^{-2})$. In the limit of $\xi_M = \xi_D = X_f = 0$ we find $\frac{f\sum_{O(\Lambda^{-1})}}{f\sum_{O(\ln(\Lambda))}} = -\frac{X^2-1}{\Lambda[\ln(2\Lambda)-1]}$ and $\frac{f\sum_{O(\Lambda^{-2})}}{f\sum_{O(\ln(\Lambda))}} = -\frac{2X^4-8X^2+1}{4\Lambda^2[\ln(2\Lambda)-1]}$; thus the ratio $\frac{X^2}{\Lambda}$ determines the importance of higher order corrections for $X \gg 1$. We take $\Lambda = 2(\beta X)^2$ for the cutoff in the following. Already for $\beta = 2$ and a maximal momentum $X = X_{\max} = 6$, the corrections of order $O(\Lambda^{-1})$ are 2% of order $O(\ln(\Lambda))$, while contributions of order $O(\Lambda^{-2})$ are smaller than 0.1%. A modest cutoff $2 \leqslant \beta \leqslant 5$ works best for comparing Eq. (22) to numerical data, as the latter is only given over a finite range of $\Omega$. A larger $\Lambda$ makes it necessary to extrapolate the data, providing a source for errors.
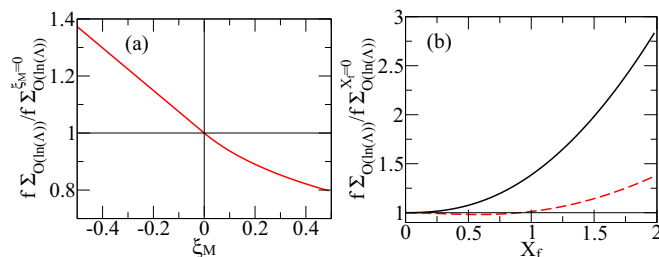


FIG. 2. (Color online) (a) Ratio $\frac{f\sum_{\mathcal{O}(\ln(\Lambda))}}{f\sum_{\mathcal{O}(\ln(\Lambda))}^{\xi_M=0}}$ of the lowest order $f$-sum rule including mass over the one without mass. $\xi_D = 0$ and $X_f = 0$. (b) Ratio $\frac{f\sum_{\mathcal{O}(\ln(\Lambda))}}{f\sum_{\mathcal{O}(\ln(\Lambda))}^{X_f=0}}$ of the lowest order $f$-sum rule including finite doping over the one without doping, $\Omega_f > 0$ ($\Omega_f < 0$) as a black, solid (red, dashed) line. $\xi_M = 0$ and $\xi_D = -0.5$. $\beta = 2$ and $X_{\max} = 6$ in both plots.

### 4. Influence of finite $\xi_M$, $\xi_D$, and $X_f$

Next, we investigate changes to the $f$-sum rule and therefore to the total spectral weight by varying the mass. The influence of a finite mass is studied in Fig. 2(a) for $\xi_D = 0$ and $X_f = 0$. A positive mass lowers the $f$-sum rule, while a negative mass increases it linearly. This is a direct consequence from the change of the overlap factor: a negative mass enhances the coupling between the two bands, while a positive mass diminishes it, as in the latter case the pseudospins do not match. It is also consistent with the increase in the optical conductivity observed in the undoped limit with negative mass [9].

Last, we consider the effects of finite doping. It blocks interband transitions close to the Dirac point, but due to the small density of states, these transitions carry only a small spectral weight. On the other hand, doping enables intraband transitions, which carry a large spectral weight due the combined effects of larger overlap factor, density of states, and smaller excitation energies compared to interband transitions. Therefore, finite doping usually increases the $f$-sum rule, as seen in Fig. 2(b), where we plot $\frac{f\sum_{O(\ln(\Lambda))}}{f\sum_{O(\ln(\Lambda))}^{X_f=0}}$ for positive (black, solid line) and negative (red, dashed line) doping with $\xi_D = -0.5$ and $X_M = 0$. A finite $\xi_D$ adds a term $\pm\frac{g_s}{4}|\xi_D|X_f^2 X^2$ to the leading order of the $f$-sum rule, $+$ ($-$) for positive (negative) doping. It can be seen as an increased (decreased) contribution from the 2DEG part of the spectrum, Eq. (21), and leads to the slight decrease of the $f$-sum rule for negative doping in panel (b).

### 5. Comparing the spectral weight of excitations

In order to compare the importance of different excitations in the system, one should compare their spectral weight and thus their contribution to the $f$-sum rule. The latter has the benefit of being independent of the Coulomb interaction strength and of the position of the excitation peaks, in contrast to the polarization function $\Pi_{rpa}^{Im}$. As an example, we assume that the excitation spectrum, $\Pi_{rpa}^{Im}$, is governed by a single plasmonic peak following a Lorentzian shape with width $\Gamma$ and peak height $\frac{1}{c\Gamma}$. Then the $f$-sum rule is proportional to

$$\int_0^\infty d\Omega\, \Omega \frac{1}{c} \frac{\Gamma}{\Gamma^2+(\Omega-\Omega_p)^2} = \frac{\Omega_p}{c}\int_0^\infty \frac{d\Omega}{\Omega_p} \frac{\Omega}{\Omega_p} \frac{\frac{\Gamma}{\Omega_p}}{(\frac{\Gamma}{\Omega_p})^2+(\frac{\Omega}{\Omega_p}-1)^2}.$$

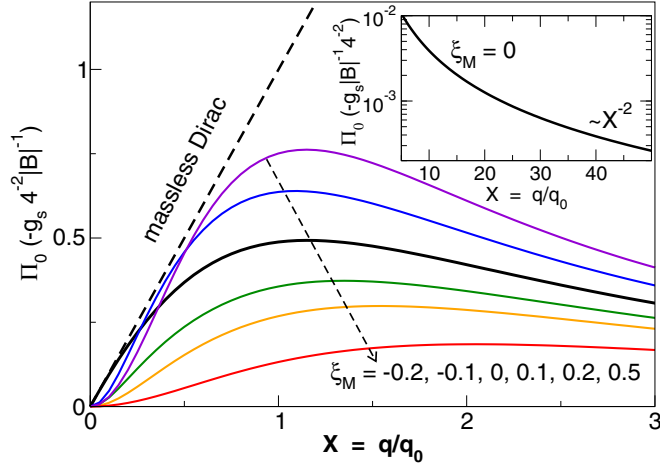The value of this integral should be independent of $\alpha$ and thus of $\Omega_p$.

FIG. 3. (Color online) Static intrinsic polarization function of the BHZ model for variable $\xi_M$ and $\xi_D = 0$.



FIG. 4. (Color online) Static intrinsic polarization function of the BHZ model for a finite $\xi_D$ value.

Therefore we find $c \propto \Omega_p$, such that the peak height of a resonance in $\Pi_{rpa}^{Im}$ naturally has to scale with $1/\Omega_p$ to fulfill the $f$-sum rule.

We conclude that the importance of a resonance in $\Pi_{rpa}^{Im}$ should be judged by its spectral weight, which can be estimated by multiplying the peak height with its position $\Omega_p$. The relevant width of the peak is given by $\frac{\Gamma}{\Omega_p}$, with $\Gamma$ being the width of the resonance in $\Pi_{rpa}^{Im}$.

### III. UNDOPED SYSTEM

In this section, we focus on an intrinsic (undoped limit $\mu = 0$) BHZ model system. First, we analyze the static polarization function and the static screening properties. Then we consider the long-wavelength limit of the dynamical polarization function, providing an analytical expansion. Finally, we add some complementary arguments elucidating the origin of the new interband plasmon (absent both in the Dirac and 2DEG cases), whose appearance for the intrinsic BHZ model has been proposed in Ref. [9].

#### A. Static limit

In order to set a reference with a closely related and analytically solvable model, we discuss the static intrinsic polarization for a massive Dirac limit, given by [27,28]

$$\Pi_0(q) = \frac{-gq}{8\pi A} \left[ \frac{1}{\chi} + \left( 1 - \frac{1}{\chi^2} \right) \arctan \chi \right] \xrightarrow{\chi \to \infty} \frac{-gq}{16A}, \quad (23)$$

where the index 0 stands for intrinsic limit $\mu = 0$, $g$ accounts for possible spin and band degeneracy, and $\chi = \frac{Aq}{2M}$. When the Dirac system is massless ($M = 0$), $\Pi_0(q)$ is a linear function of the momentum $q$. A finite Dirac mass suppresses the polarization for $q \lesssim M/A$, where $\Pi_0(q)$ shows a superlinear behavior. For $q \gg M/A$, the mass is negligible instead and the result of the massless limit is reproduced.

The static polarization function of the BHZ model is simply obtained by direct numerical evaluation of Eq. (5) at zero frequency. In Fig. 3, we show $\Pi_0(X)$ calculated for a particle-hole symmetric BHZ system ($\xi_D = 0$). Note that we obtain the
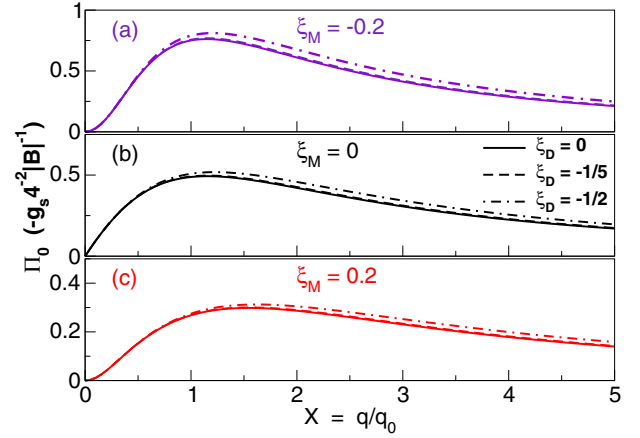
massless Dirac case in the limit $B \to 0$ (and therefore $X \to 0$), where $\lim_{X \to 0} |B| \Pi_0(X)/X = -\frac{g_s}{16}$. A finite $B$ parameter determines a fundamental qualitative change with respect to a Dirac system. Indeed, $\Pi_0(X)$ reaches a maximum at $X \approx 1$ and then decays as $1/X^2$ for $x \gg 1$ as shown in the inset of Fig. 3. A finite and positive Dirac mass $M$ leads to a general suppression of the polarization function with respect to the massless case. In the region $X < 1$ (where quadratic terms are less important), $\Pi_0(X)$ resembles the massive Dirac case, with a superlinear increase in the region $X \lesssim \xi_M$, due to the suppression of the interband overlap factor determining a reduction of the polarization at small momentum. For intermediate values $\xi_M \lesssim X \lesssim 1$, analogously to the massive Dirac limit, $\Pi_0(X)$ is approximatively linear in $X$. Considering larger momenta $X \gtrsim 1$, the behavior is dominated by the quadratic terms and the polarization eventually vanishes for $X \to \infty$. In general, the interplay of quadratic terms and a finite Dirac mass shifts the maximum of $\Pi_0(X)$. When the Dirac mass $M$ is negative (topological insulator phase), we observe a less pronounced suppression of the polarization for $X < \xi_M$, with respect to a massive Dirac system (normal insulator) with equal modulus of $M$. Moreover, on the contrary to the $M > 0$ case, $\Pi_0(X)$ is enhanced at large $X$ with respect to the massless, particle-hole symmetric limit. This behavior is due to the enhanced overlap factor between electron and hole bands in the TI phase.

In Figs. 4(a)–4(c), we analyze the effects of a finite value of the parameter $\xi_D$ in the BHZ model, for $\xi_M = -0.2$, 0, and 0.2. A finite $\xi_D$ breaks particle-hole symmetry by changing the effective masses of conduction and valence bands. We only found quantitative changes to $\Pi_0(X)$, which is progressively reduced for increasing $\xi_D$.

#### B. Screening

In a massless Dirac system, where the static polarization is linear in $q$ [Eq. (23)], the dielectric function is a constant,

$$\varepsilon(q) = \varepsilon_r \left( 1 + \frac{g_s g_v \pi}{8} \alpha \right) \equiv \varepsilon; \quad (24)$$

therefore the intrinsic polarization contribution can be absorbed into an effective background dielectric constant $\epsilon$. As

a consequence, a test charge $Ze$, placed at the origin, induces a screening electronic density

$$Ze\left[n_0(\boldsymbol{q}) + n_r\right] = Ze\left(\frac{1-\varepsilon}{\varepsilon}\right),$$

which in real space corresponds to a screening image charge [a fraction $(1-\varepsilon)/\varepsilon$ of the external one] placed exactly at the same position,

$$n(\boldsymbol{r}) = -\left(\frac{1-\varepsilon}{\varepsilon}\right)\delta(\boldsymbol{r}). \tag{25}$$

Note that the screening charge only due to the electronic system (without background contribution) is a fraction $-(\epsilon - \epsilon_r)/\epsilon\epsilon_r$ of the external one.

In a massive Dirac system, the large $q$ behavior of $\Pi_0(q)$ reproduces the massless limit and therefore a screening charge given by Eq. (25) is also developed at vanishing distances $r$ in response to an external test charge. However, in the long-wavelength limit ($q < M/A$) $\Pi_0(q)$ has a superlinear behavior and thus $n_0(0) \propto \lim_{q\to 0}\Pi_0(q)/q = 0$. Thus an induced charge density of the same sign as the external charge is developed at finite distances [27] [summing up to $Ze(\epsilon - \epsilon_r)/\epsilon\epsilon_r$], so that the test charge feels only the background screening over long distances, as expected in an insulator.

For the BHZ model, we find similarly to Eq. (24)

$$\lim_{X\to 0}\varepsilon(X) = \varepsilon_r\left(1 + \frac{g_s\pi}{8}\alpha\right) \tag{26}$$

in the long-wavelength limit, but $\lim_{X\to\infty}\varepsilon(X) = \varepsilon_r$. This fact is reflected in the real space behavior of the induced charge density, which is given by

$$n_0(r) = \eta_0 \int dX\, J_0(Xrq_0)\frac{|B|\Pi_0(X)}{1 - \alpha g_0(X)} \tag{27}$$

with $\eta_0 = \frac{\alpha}{\epsilon_r}q_0^2$ a natural charge density constant of the model. We note that $n_0(r)$ is proportional to $q_0^2$ and $\alpha$, but $n_0(r)$ has an additional dependence on $\alpha$ (and thus on $A$) through its integrand. It also parametrically depends on $\xi_M$ and $\xi_D$ through $\Pi_0(X)$ and $g_0(X)$.

In Fig. 5, we plot the induced charge density $n_0(r)$ in real space for $\xi_D = \xi_M = 0$ with different values of $\alpha$. Opposite to a Dirac system, the induced charge density has a finite extent over a distance of the order of $1/q_0$, which is clearly related to the decay of $\Pi_0$ at large wave vector due to the presence of quadratic $B$ terms. $n_0(r)$ decays at large distances as $r^{-2}$. An electron far away from this induced charge, $r \gg 1/q_0$, does not see the finite extent of it and is therefore screened in the same way as in the Dirac system, leading to the similarity of Eqs. (24) and (26). In the opposite limit where the electron sits on top of the induced charge, $r \ll 1/q_0$, it does not feel it at all, resulting in no screening besides $\varepsilon_r$.

In the inset of Fig. 5, we study the effect of a finite Dirac mass term. With a finite $\xi_M$, the induced density (as in the case of pure Dirac systems) shows a qualitatively different behavior. $n_0(r)$ changes sign for sufficiently large $r$, ensuring a vanishing total induced charge. From a quantitative point of view, a finite negative (positive) $M$ enhances (suppresses)
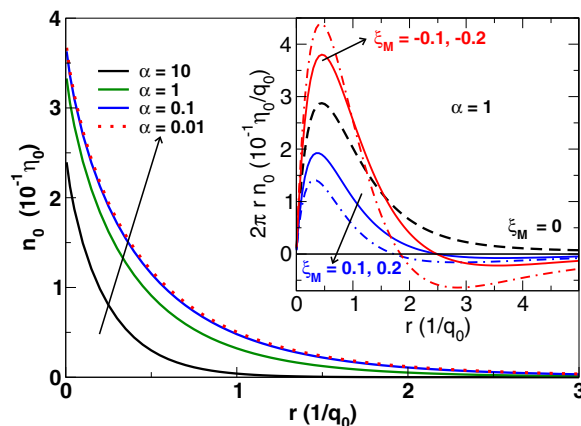


FIG. 5. (Color online) Induced charge $n_0(r)$ due to a test charge in the intrinsic limit of the BHZ model for $\xi_D = \xi_M = 0$. The plot is invariant under a change of $B$ parameter and only depends on the effective fine structure constant $\alpha$. In the inset, $r\, n_0(r)$ calculated for $\alpha = 1$ and finite Dirac mass.

the features of $n_0(r)$, due to its effect on the interband overlap factor.

### C. Long-wavelength expansion

An analytic discussion of the polarization function is only possible in the limit $X \to 0$. Here, we focus on the limit of vanishing mass $\xi_M \to 0$ to extract an analytic formula of the plasmon dispersion. An expansion of $\Pi^R$ in $X$ gives, for $\Omega > X$,

$$\begin{aligned}
\Pi^R = {}& -\frac{g_s}{8|B|}X^2\left(2\frac{\Omega - \sqrt{1+\Omega^2}\,\mathrm{ArcSinh}(\Omega)}{\pi\Omega^3}\right.\\
&\left. + i\,\frac{1}{\Omega(1+\sqrt{1+\Omega^2})}\right) + O(X^4)\\
\underset{\Omega\gg 1}{=}{}& -\frac{g_s}{8|B|}\frac{X^2}{\Omega^2}\left(2\frac{1 - \ln(2) - \ln(\Omega)}{\pi} + i\right)\\
&+ O(\Omega^{-3}) + O(X^4),
\end{aligned} \tag{28}$$

where one finds an $\Omega^{-2}$ behavior with an additional logarithmic correction for the real part in the high-frequency limit.

Calculating the plasmon dispersion by performing an expansion of Eq. (10) up to second order in $\frac{\Gamma}{\Omega}$, one finds the linear dispersion

$$\Omega_p = \tfrac{1}{8}\pi g\alpha X + O(X^2), \tag{29}$$

which is only valid for sufficiently large $\alpha$, such that the conditions $\mathrm{Re}[\Pi^R(X,\Omega_p)] > 0$ and $\Omega > X$ are fulfilled. The linearity of the dispersion follows from Eq. (28) only by inclusion of the damping via $\Gamma$. Without the substitution $\Omega \to \Omega - i\Gamma$, $\mathrm{Re}[\varepsilon(X,\Omega_p)] = 0$ has no sensible solution for $\Omega_p$. The damping ratio is given by

$$\frac{\Gamma}{\Omega} \underset{\Omega\ll 1}{=} 1 - \frac{\Omega^2}{8} + O(\Omega^3), \tag{30}$$

underlining the importance of damping in this limit. The plasmon is only well defined for a finite $\Omega_p > \Omega_c$, with
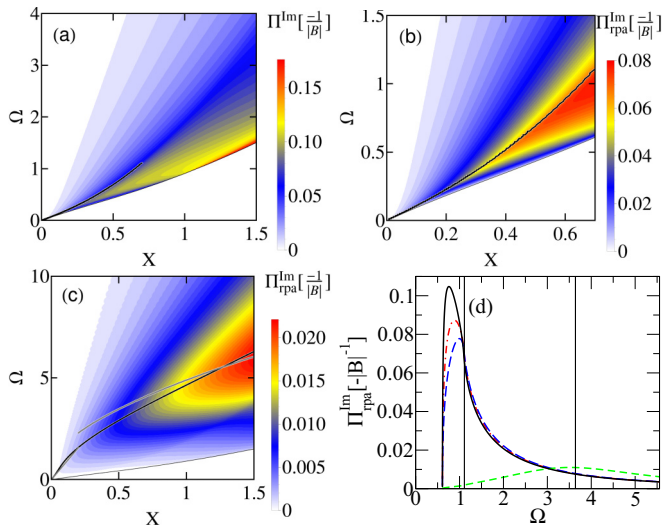
FIG. 6. (Color online) Plots of $\Pi^{Im}$ (a) and $\Pi_{rpa}^{Im}$ for $\alpha = 0.4$ (b) and $\alpha = 10$ (c). (d) shows line cuts for fixed $X = 0.7$ with $\alpha \in \{0, 0.2, 0.4, 10\}$ in black solid, red dot-dashed, blue long-dashed, and green short-dashed lines, respectively. $\xi_M = 0$ and $\xi_D = -0.5$.

$\frac{\Gamma}{\Omega}\big|_{\Omega=\Omega_c} \lesssim c$ where $0 < c < 1$ sets the limit for the detectability of the plasmons; for example in the recent experiment [24] $c$ was shown to be of the order 0.5. Equation (29) translates this into a finite momentum scale $q > \frac{q_0}{g\alpha}\frac{8\Omega_c}{\pi}$ with the intrinsic plasmon length scale $l_0 = \frac{g\alpha}{q_0}$, given by the Coulomb interaction strength times the charge decay length $\frac{1}{q_0}$; see Sec. III B. We interpret $l_0$ as the length scale up to which charge separation due to Coulomb interaction can occur and give rise to the interband plasmons, in an undoped and therefore overall neutral system.

In the opposite limit of high frequencies, the term $\ln(\Omega)$ spoils a simple $\sqrt{X}$ behavior of the plasmon dispersion. In this limit, we can extract the analytic form of the damping rate

$$\frac{\Gamma}{\Omega} \underset{\Omega \gg 1}{=} \frac{1}{3\pi}\left[ -\ln\left(\frac{4\Omega^2}{e^3}\right) + \sqrt{3\pi^2 + \ln\left(\frac{4\Omega^2}{e^3}\right)^2} \right]$$
$$+ O\left(\frac{1}{\Omega}\right)$$
$$\underset{\Omega \to \infty}{=} \frac{\pi}{2\ln\left(\frac{4\Omega^2}{e^3}\right)} \tag{31}$$

with Euler's number $e$, yet the plasmon dispersion can only be calculated numerically.

In the following discussion of the different excitation spectra, we will use these analytic results to check our numerics in the limits of small momenta and low and high frequencies.

### D. Excitation spectrum

The noninteracting single-particle excitation spectrum is given by $\Pi^{Im}$, which we plot in Fig. 6(a) for $\xi_M = 0$ and $\xi_D = -0.5$. Due to energy conservation, there are no excitations beneath a frequency $\Omega_{min}$. In contrast to graphene, where one observes a diverging behavior of the polarization at $\Omega_{min}$, here $\Pi^{Im}$ increases continuously from 0. This is due to the broken

particle-hole symmetry ($\xi_D < 0$) which ensures that the lowest energy excitations correspond to processes exciting particles from the valence band to the proximity of the Dirac point, where, however, the density of states is zero. The excitation spectrum shows a maximum for small momenta $X < 1$ which lies beneath the plasmon dispersion given by the black line, perturbatively calculated from Eq. (10) up to order $(\frac{\Gamma}{\Omega})^2$ for $\alpha = 0.4$.

Considering a finite Coulomb interaction, the excitation spectrum is given by $\Pi_{rpa}^{Im}$ plotted in Fig. 6(b) for $\alpha = 0.4$ and Fig. 6(c) for $\alpha = 10$. The maximum of the spectrum shifts to higher energies compared to the noninteracting one, indicating the formation of a collective excitation in the system, i.e., a plasmon. This is proven by solving the plasmon equation [Eq. (10)] perturbatively up to order $(\frac{\Gamma}{\Omega})^2$, with the dispersion plotted as a black line on top of the spectrum. Additionally, the dispersions based on the expansion of $\Pi^R$ in the limit $X \to 0$ for $\Omega \ll 1$ and $\Omega \gg 1$ are plotted as gray lines in Fig. 6(c).

The plasmon dispersion relation starts linearly for small $q$, as one would expect for a neutral system without doping. At high energies on the other hand, a free-particle behavior could be expected, leading to the usual $\sqrt{q}$ dispersion known from doped systems. Although Eq. (28) shows that this picture is only partly true due to the logarithmic correction of $\Pi^{Re}$, Fig. 6(c) indicates a qualitative agreement.

Figure 6(d) shows line cuts of $\Pi_{rpa}^{Im}$ for fixed $X = 0.7$ with $\alpha \in \{0, 0.2, 0.4, 10\}$. Additionally, the black vertical lines indicate the plasmon frequency for $\alpha \leqslant 0.4$ (left line) and $\alpha = 10$ (right line). For $\alpha = 0.2$ the maximum of the interacting spectrum lies between the maximum of the noninteracting spectrum and the plasmon frequency, indicating that single-particle and collective excitations are equally strong. Increasing the interaction to $\alpha = 0.4$, the maximum of the interacting spectrum and the plasmon frequency almost coincide; therefore the plasmon dominates over the single-particle excitation. At very large interactions $\alpha = 10$, the plasmon is the only relevant excitation in the system.

Increasing the Coulomb interaction broadens the plasmon peak and reduces its height as shown in Fig. 6(d). This seems contrary to the picture of a plasmon as a sharp interaction-induced charge resonance, suggesting that these interband plasmons may not be well defined for high energies. Yet this is a false conclusion. In Sec. II G 5 we discussed that the contribution of the resonance to the $f$-sum rule is the actual measure of importance of a resonance. It can be estimated by multiplying the peak height in $\Pi_{rpa}^{Im}$ by $\Omega_p$, while the relevant peak width is given by $\frac{\Gamma}{\Omega_p}$. The latter is decreasing with $\Omega_p$ according to Eq. (31). From this normalization of the peak we conclude that the discussed interband plasmons fulfill the interpretation as sharp interaction-induced charge resonances, with the width $\frac{\Gamma}{\Omega_p}$ decreasing with increasing plasmon frequency, above the critical frequency $\Omega_c$ as defined in Sec. III C.

### E. $f$-sum rule

The $f$-sum rule provides a check for our numerics. In Fig. 7 we plot the ratio $\frac{\Delta_{f\Sigma}^{num}}{f\Sigma}$, with $\Delta_{f\Sigma}^{num} = f\Sigma^{num} - f\Sigma$ where $f\Sigma^{num}$ is the numerical calculated $f$-sum rule and
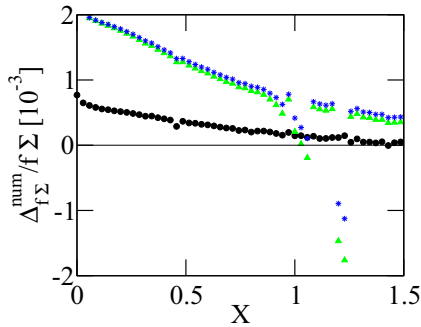
FIG. 7. (Color online) The ratio $\frac{\Delta^{num}_{f\Sigma}}{f\Sigma}$, with $\Delta^{num}_{f\Sigma}$ being the difference between the numerical and analytical $f$-sum rule. Black dots are for the noninteracting spectrum, while blue stars stand for $\alpha = 0.4$ and green triangles for $\alpha = 10$. $\beta = 3$, $X_{max} = 6$, $\xi_M = 0$, and $\xi_D = -0.5$. The deviations around $X \gtrsim 1$ stem from numerical instabilities, which are however negligibly small.

$f\sum$ the analytic one. The deviation are of the order $10^{-3}$, comparable to the analytical uncertainty, see Sec. II G, and thus negligible. The $f$-sum has to be the same for interacting and noninteracting systems. We find a slight dependence on the interaction strength $\alpha$, which could be a numerical artifact, depending on $\Lambda$, or a real $\alpha$ dependence like in graphene, where spectral weight is missing for small frequencies; cf. Eq. (14) in Ref. [26] ($\Pi^{RPA} < \Pi^R \; \forall q,\omega$ for the undoped Dirac model). As the effect declines with increasing cutoff $\Lambda$, we conclude that the RPA approximation in the BHZ model misses no spectral weight compared to the full Coulomb interaction, even in the undoped limit.

## IV. DOPED SYSTEM

In this section, we extend our analysis to finite doping $\mu > 0$, where a net charge density is present in the system. Doping the system has two effects: one is the Fermi blocking of interband excitations [red arrow in Fig. 12(a)] for small $X$ and $\Omega$. The other is the appearance of intraband excitations [green arrow in Fig. 12(a)], which are absent in the intrinsic limit. Again, first we study the polarization and screening properties of the system in the static limit, where we also study Friedel oscillations due to the scattering on a charged impurity. Then, we study the dynamical polarization function in the long-wavelength limit, where we obtain an analytical expression for the collective plasmonic modes of the system. Finally we numerically compute the dynamical polarization function in the full range of momenta and frequencies in the full parameter space of the BHZ model, analyzing the effect of each of the model parameters. Particular emphasis is put on the coexistence of interband and intraband plasmons and on how the BHZ model interpolates between the Dirac and 2DEG behavior.

### A. Static limit

In Fig. 8, we present the static polarization function $\tilde{\Pi}(X) = \Pi(X)/G(\mu)$ at finite doping, conveniently normalized by the density of states at the Fermi level $G(\mu)$. This normalization stands out naturally from the long-wavelength property of the
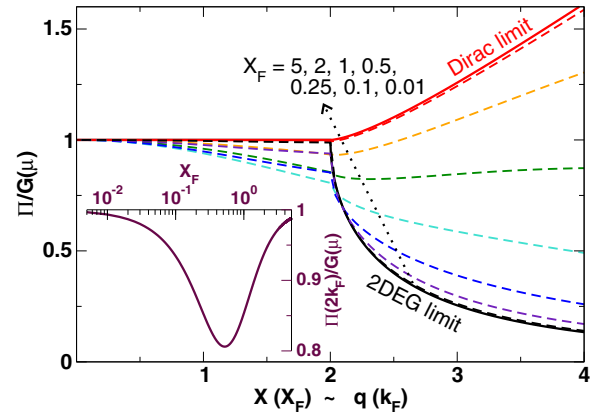


FIG. 8. (Color online) Static polarization function $\tilde{\Pi}(X)$ of the BHZ model for $\xi_M = \xi_D = 0$ at finite doping for different value of $X_F$, normalized by the DOS $G(\mu)$. In the inset, details on the value of $\Pi(2X_F)$ as a function of $X_F$ are given.

polarization function

$$\lim_{q\to 0} \Pi(q) = \Pi_\mu(0) = G(\mu). \tag{32}$$

For the BHZ model at finite doping, $\tilde{\Pi}(X)$ has a pronounced dependence on the extrinsic parameter $X_F = k_F/q_0$. For $X_F \ll 1$ ($X_F \gg 1$) the Fermi level falls in a region where locally the dispersion curve has predominant Dirac (2DEG) character. In a 2DEG system, the static polarization assumes the following analytic form [29],

$$\tilde{\Pi}(q) = 1 - \Theta(q - 2k_F)\frac{\sqrt{q^2 - 4k_F^2}}{q}, \tag{33}$$

while in the Dirac limit we have [30,31]

$$\tilde{\Pi}(q) = 1 - \Theta(q - 2k_F)$$
$$\times \left[ \frac{\sqrt{q^2 - 4k_F^2}}{2q} - \frac{q}{4k_f}\arctan\frac{\sqrt{q^2 - 4k_F^2}}{2k_F} \right]. \tag{34}$$

Our calculations for the BHZ model with $\xi_M = \xi_D = 0$ correctly reproduce the Dirac and 2DEG limits for $X_F \ll 1$ and $X_F \gg 1$, respectively. We note that with a finite $B$ term and nonzero $X_F$ the polarization will always have a decay behavior for $q > q_0$. In the 2DEG and Dirac limit one finds $\tilde{\Pi}(q) = 1$ for $q < 2k_F$, coincidence due to the balancing effect of dispersion curve and overlap factor. Interestingly, in the BHZ model we observe instead a deviation from unity, shown in details in the inset of Fig. 8, which has a maximum for $X_F \approx 0.5$. In the 2DEG limit, $X_F \gg 1$, $\tilde{\Pi}(X)$ has a strong discontinuity in its first derivative at $X = 2X_F$, while for decreasing $X_F$ this discontinuity decreases and finally vanishes in the Dirac limit, where the discontinuity affects only the second derivative.

### B. Screening

We already analyzed in Sec. III B the intrinsic response of a BHZ system to a test charge, when no net charge density is present in the system. While the intrinsic response is realized on intrinsic scales of the model $1/q_0$, the "metallic" response
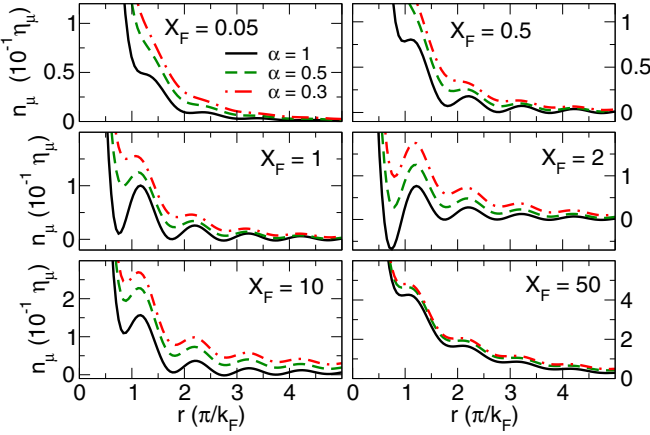
FIG. 9. (Color online) Induced charge density in real space for the BHZ model for $\xi_M = \xi_D = 0$ and $\alpha = 0.3$, 0.5, and 1. Data in different panels belong to systems with $X_F = 0.05$, 0.5, 1, 2, 10, and 50. All calculation are obtained by keeping $\epsilon_r = 10$ and $k_F = 0.1$ nm$^{-1}$, and varying $A \approx 0.143$, 0.29, and 0.47 eV nm, for $\alpha = 0.3$, 0.5, and 1, respectively, while varying the parameter $B$ accordingly to $X_F$. In the panel $X_F = 50$ (2DEG limit), the three curves with $\alpha = 0.3$, 0.5, and 1 are quite close and correspond to similar $\beta$ parameter ($\beta = 0.01$, 0.008, and 0.007, respectively).

(at finite electronic density) is characterized by the Fermi wave length $\pi/k_F$. Therefore it is convenient to express $n_\mu(X)$ as a function of dimensionless units $\tilde{X} = X/X_F = k/k_F$, due to the presence of a discontinuity at $\Pi_\mu(2X_F)$. The induced charge density $n_\mu$ is given by

$$n_\mu(r) = \eta_\mu \int d\tilde{X} \, \frac{J_0(rk_F\tilde{X})}{1 - \alpha g_0(\tilde{X}X_F)} \frac{\tilde{\Pi}_\mu(\tilde{X}X_F)}{1 - \alpha g(\tilde{X}X_F)}, \quad (35)$$

where, using the property Eq. (32), we have emphasized the dependence of the induced density on the DOS at the Fermi level, which now appears in the scaling factor $\eta_\mu = \eta_0 |B| G(\mu) X_F = \frac{e^2 k_F}{4\pi\epsilon_0\epsilon_r^2} G(\mu)$. We note that the integral also depends on the parameters $\alpha$ and $X_F$ (and naturally on $\xi_M$ and $\xi_D$, when finite).

In Fig. 9, we present the induced screening electronic radial density for the BHZ model for $\xi_M = \xi_D = 0$ due to a pointlike test charge. Each panel corresponds to a different value of the ratio $X_F = k_F/q_0$, and within each panel curves differing by the Dirac fine structure constant $\alpha$ are presented. Friedel oscillations appear of period $\pi/k_F$, which become more defined for larger $\alpha$. We also note that density oscillations are more prominent for $k_F \approx q_0$ than in the Dirac ($X_F \ll 1$) and 2DEG limits ($X_F \gg 1$). In the 2DEG limit the $\alpha$ parameter is ill defined and should be replaced by the more general parameter $\beta = \frac{e^2 G(\mu)}{2\epsilon_0\epsilon_r k_F}$, characterizing the dielectric response of the system.

The presence of Friedel oscillations and their asymptotic behavior are related through the Lighthill theorem [32] to discontinuities in the static polarization function and its derivatives (see for example Ref. [33] for a detailed discussion). A discontinuity like $|q - 2k_F|^\nu \Theta(q - 2k_f)$ in $\Pi(q)$, with $\Theta$ the Heaviside step function and $\nu \in \mathbb{R}$, translates into a decay of the oscillations in $n(r)$ with leading order $r^{-\nu-3/2}$. One finds $\nu = 1/2$ ($\nu = 3/2$) for the leading order discontinuity

of a 2DEG (Dirac) system, such that the first (second) and all higher derivatives of the static polarization function are discontinuous at $q = 2k_F$. Analyzing the Friedel oscillations for the BHZ model, one finds a composition of two different contributions with an asymptotic decay at large distances as $r^{-2}$ (2DEG contribution) and $r^{-3}$ (Dirac contribution), respectively. As a consequence, the discontinuity in the RPA polarization function of the BHZ model at $q = 2k_F$ can be very well approximated by a combination of 2DEG ($\nu = 1/2$) and Dirac ($\nu = 3/2$) contribution. In the Dirac (2DEG) limit, the effect of the discontinuity in the second (first) derivative becomes predominant and oscillations purely decay in leading order as $r^{-3}$ ($r^{-2}$).

### C. Long-wavelength expansion, plasmon dispersion

At finite doping, for small momenta $X$, the polarization function is governed by intraband excitations, as the interband excitations are Fermi-blocked. We perform an expansion in this limit, for $\Omega > X$, to gain an analytical insight into the physics at finite doping and derive an analytical formula for the plasmon dispersion. In particular, intraband plasmons are expected to be the dominant excitation for small momenta, similarly to the 2DEG and Dirac case. We expand the polarization function up to order $X^4$,

$$|B|\text{Re}[\Pi^R(X,\Omega)] = \Pi_{44}\frac{X^4}{\Omega^4} + \Pi_{42}\frac{X^4}{\Omega^2} + \Pi_{40}X^4$$
$$+ \Pi_{22}\frac{X^2}{\Omega^2} + \Pi_{20}X^2 + O(\Omega^2),$$

and use it to solve Eq. (10). We obtain the plasmon dispersion

$$\Omega = \sqrt{2\pi\alpha\Pi_{22}}\sqrt{X} + \left(\frac{\Pi_{44}}{\Pi_{22}^{\frac{3}{2}}}\frac{1}{\sqrt{8\pi\alpha}} + \sqrt{2\pi^3\alpha^3\Pi_{22}}\Pi_{20}\right)X^{\frac{3}{2}}$$
$$(36)$$

with the leading coefficient

$$\Pi_{22} = g_s\Theta(X_f)\left(\frac{X_f^2(1 + 2X_f^2 + 2\xi_M)}{4\pi\sqrt{X_f^2 + (\xi_M + X_f^2)^2}} - \gamma\xi_D\frac{X_f^2}{2\pi}\right)$$

$$= g_s\Theta(X_f)\frac{1}{4\pi}\left(|\Omega_f| + \underbrace{\Pi_{\text{inter}}(X_f)}_{-|\xi_M| < \ldots < |\Omega_f|}\right)$$

$$\underset{\substack{\xi_M=0 \\ X_f\to0}}{=} g_s\frac{X_f}{4\pi} + O(X_f^2) = g_s\frac{|\Omega_f|}{4\pi} + O(X_f^2) \quad (37)$$

$$\underset{\substack{\xi_M=0 \\ X_f\to\infty}}{=} g_s\frac{X_f^2}{2\pi}(1 - \gamma\xi_D) + O\left(\frac{1}{X_f^2}\right) = g_s\frac{|\Omega_f|}{2\pi} + O\left(\frac{1}{X_f^2}\right)$$

$$(38)$$

with $\gamma = \text{sgn}[\Omega_f]$ and $\Pi_{\text{inter}}(X_f) = \frac{X_f^4 - \xi_M^2}{\sqrt{X_f^2 + (\xi_M + X_f^2)^2}} - \gamma\xi_D X_f^2$. In the limit of zero mass, $\Pi_{\text{inter}}(X_f)$ interpolates smoothly between 0 for $X_f \to 0$ and $|\Omega_f|$ for $X_f \to \infty$. The former case corresponds to the Dirac limit, where one finds

the plasmon frequency

$$\omega = A\sqrt{\frac{g\alpha k_f}{2}}\sqrt{q} = \sqrt{\frac{ge^2\mu}{8\pi\varepsilon_0\varepsilon_r}}\sqrt{q}$$

in the literature [10], being identical to Eqs. (36), (37). The latter case is the 2DEG limit, where one finds the plasmon dispersion

$$\omega = \sqrt{\frac{e^2 N}{2m\varepsilon_0\varepsilon_r}}\sqrt{q} = \sqrt{\frac{ge^2\mu}{4\pi\varepsilon_0\varepsilon_r}}\sqrt{q}$$

in the literature [29], with $N = \frac{g}{4\pi}k_f^2$ the carrier density and $m = \frac{1}{2|B+D|}$. This is in agreement with Eqs. (36), (38).

Thus the BHZ model as a function of its parameters reproduces the plasmon dispersion in the Dirac and 2DEG limits and interpolates between them. We note that for $k_f \to 0$ the term $\Pi_{22}$ is zero and the intraband plasmon disappears. In this limit, the leading order contribution $O(\frac{X^2}{\Omega^2})$ of the intrinsic polarization, Eq. (28), takes the place of $\Pi_{22}$. The crucial difference between the extrinsic and the intrinsic polarization is that the latter has a finite imaginary part of order $O(\frac{X^2}{\Omega^2})$, leading to the linear dispersion of the interband plasmons. Yet for finite $k_f > 0$, these interband plasmons are suppressed due to the Fermi blockade of the interband excitations and only exist if their plasmon frequency exceeds both the chemical potential $\Omega_f$ and the critical frequency $\Omega_c$ as defined in Sec. III C; see for example Fig. 14.

Besides the different scaling with momenta in the limit $q \to 0$, also the scaling with $\alpha$ is different for the inter- and intraband plasmons, Eqs. (29) and (36): linear versus square root. This will have important consequences in the following when we will discuss how to separate the two different collective excitations.

### D. Excitation spectrum: Interpolation between Dirac and 2DEG regime

We begin the discussion of the doped spectrum by looking at the limiting results of the 2DEG and Dirac systems. From this, we then find that we can interpolate between them by changing the Fermi momentum. Interestingly, by considering the cases of broken particle-hole symmetry and large masses, we also find regimes which are distinct from the Dirac and 2DEG limit. As an example, these regimes support both inter- and intraband plasmons at parameters which are realistic for HgTe QWs.

In all the following plots, the boundaries of the single-particle spectrum will be indicated by faint black lines, the isolines $\Pi^{Re} = 0$ by red lines. The plasmon dispersions are plotted as black curves (full result from perturbation theory) and gray curves (expanded result in limit $X \to 0$).

#### 1. Limiting case: 2DEG

In the 2DEG limit, only intraband excitations are possible. The polarization function has a well-known analytical form [29]; therefore we can easily plot the noninteracting spectrum in Fig. 10(a). $\Pi^{Im}$ is peaked for $q,\omega \to 0$ closely to the upper boundary of the spectrum. It decays to zero instead for large
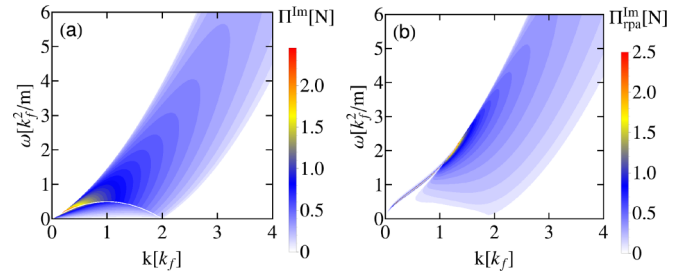


FIG. 10. (Color online) Spectrum of a 2DEG. (a) Imaginary part of $\Pi^R$ with $N = \frac{g_s m}{2\pi\hbar^2}$ and $g_s$ the degeneracy factor. (b) $\Pi_{rpa}^{Im}$ for $r_s = 2$, with $v_q = \frac{r_s k_f}{Nq}$ the Coulomb interaction. We add an artificial damping in the region of $\Pi^{Im} = 0$ to make the plasmons visible.

momenta and frequencies like $\Pi^{Im} \propto q^{-1}$, if one considers a fixed ratio $\omega \propto q^2$ within the SPE region.

The interacting spectrum is shown in Fig. 10(b). An intraband plasmon appears with the usual $\sqrt{q}$ dispersion for $q \to 0$. It absorbs all of the spectral weight in this limit; thus $\Pi_{rpa}^{Im}$ is suppressed in the SPE region. For intermediate momenta, the plasmon dispersion lies in the SPE region and the plasmon decays and broadens. For larger momenta and frequencies, the interacting and noninteracting spectra agree qualitatively.

#### 2. Limiting case: Dirac

The Dirac spectrum comprises both inter- and intraband excitations. The polarization function still has a well-known analytical expression [10,11], of which we plot the noninteracting spectrum $\Pi^{Im}$ in Fig. 11(a). The intraband excitations occur for higher energies $\omega > v_f q$, while for intraband excitations less energy is needed, $\omega < v_f q$. Both excitation spectra touch at $v_f q = \omega$, where they diverge. Only the Fermi blockade suppresses the interband transitions in $\Pi^{Im}$ for $q < 2k_f$ and cures the divergency; see Fig. 11(a) for $\omega > v_f q$. One finds a $\omega^{-1}$ decay for high frequencies.

The interacting spectrum $\Pi_{rpa}^{Im}$ is plotted in Fig. 11(b) for $\alpha = 0.6$. Similarly to the 2DEG, all of the intraband spectral weight is absorbed by a plasmon in the limit $q \to 0$ and the divergence at $v_f q = \omega$ is cured. Interestingly, for sufficient large interaction strength $\alpha$ the plasmon decays in the interband
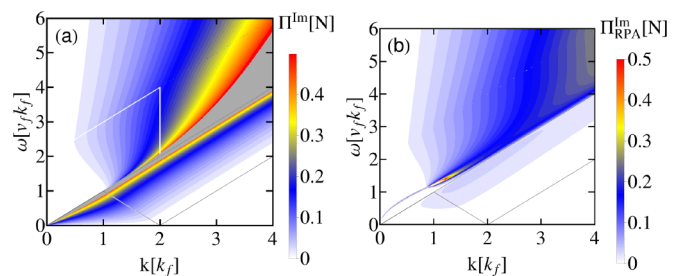


FIG. 11. (Color online) Plots for Dirac case. (a) $\Pi^{Im}$ with $N = \frac{g_s k_f}{\hbar v_f}$ and $g_s$ the degeneracy factor. In the gray area, the color scale is exceeded due to the divergency of $\Pi^{Im}$. (b) $\Pi_{rpa}^{Im}$ for $r_s = 2\pi g_s \alpha = 4\pi\, 0.6$, with $v_q = \frac{r_s k_f}{Nq}$ the Coulomb interaction. We add an artificial damping in the regions of $\Pi^{Im} = 0$ to make the plasmons visible.

spectrum. For larger momenta and frequencies, we note that the intraband polarization does not recover the noninteracting value, as it does for the 2DEG, but remains much smaller. Therefore single-particle intraband excitations are blocked altogether for all momenta and frequencies in this limit. The missing spectral weight goes into a charge resonance at higher frequencies in the interband spectrum [26]. Yet, this resonance is not a solution of the plasmon equation and therefore not a plasmon [15].

### 3. BHZ model, $\xi_M = \xi_D = 0$

The band structure of the BHZ model without mass and particle-hole symmetry breaking is shown in Fig. 12(a). The interband single-particle excitations lying lowest in energy are symmetric in momentum as shown by the red arrow in Fig. 12(a), going from $-X$ to $X$. Due to particle-hole symmetry, this leads to nesting and thus one expects these excitations to dominate the interband spectrum. Interband excitations as indicated by the dashed, black arrow on the other hand, going from momentum $X + X_f$ to $X_f$ with $X \| X_f$, are suppressed due to imperfect nesting of the different sized electron and hole cones, as well as by a small overlap factor. The latter can be cured by introducing a large negative mass, as will be shown in Sec. IV F. Then these excitations have a considerable influence on the polarization for small energies, helping with the formation of interband plasmons, following the ideas presented in Sec. II D 1. In the pure Dirac system, these processes are forbidden by helicity.

By varying the doping level we can modify the excitation spectrum of the system [see Figs. 12(b)–12(d)] to resemble that of a Dirac system ($X_f \ll 1$) or of a 2DEG ($X_f \gg 1$), or to obtain an intermediate behavior ($X_f \sim 1$). In the pictures we highlight the boundaries of the excitation spectra, with the red area corresponding to the interband spectrum and the blue area to the intraband spectrum. The overlap between the two is indicated by the purple area. The boundaries of the spectra vary from the linear graphene behavior to the $q^2$ dependence of the 2DEG. In general, the mixing of linear



FIG. 13. (Color online) Imaginary (a) and real part (b) of the polarization function for $X_f = 0.1$. The red line indicates $\Pi^{Re} = 0$.

and quadratic dispersion leads to an overlap of the inter- and intraband spectrum. This affects the visibility of the interband plasmons, which can be hidden due to strong single-particle damping.

(a) *Weak doping of $X_f = 0.1$.* The extrinsic ($k_f$) and intrinsic ($q_0$) scales of the system are separated by one order of magnitude. As the Fermi surface lies in the (almost) linear part of the spectrum, we expect that on the $k_f$ scale we resemble graphene. The physics on the $q_0$ scale on the other hand should be more or less untouched by the doping, and the system should behave as in the intrinsic limit.

We plot $\Pi^R$ in Fig. 13. Comparing panel (a) to Fig. 11, one finds good agreement with the Dirac case. The biggest deviation is found in the peak of $\Pi^{Im}$ at $\Omega_{min}^{inter}$, which is not symmetric as for a Dirac system due to the overlap of inter- and intraband spectrum [Fig. 12(b)]. The finite quadratic part in the spectrum cures the divergency formerly occurring in the Dirac limit. The real part of $-\Pi^R$ is strongly negative only at the upper boundary of the intraband spectrum. This indicates that for small interactions, only one plasmon will dominate the excitation spectrum on the Fermi scale.

As we are interested in the regime where both inter- and intraband plasmons are visible, we look at the interacting spectrum, given in Fig. 14 by plotting $\Pi_{rpa}^{Im}$, for a strong interaction $\alpha = 10$. On the Fermi scale [panel (a)], the intraband plasmon absorbs all spectral weight from the intraband spectrum. The dispersion agrees with the perturbative dispersion from the expansion in Eq. (36) in the limit $X \to 0$, plotted as a gray curve. The green, dashed line shows the linear dispersion of the interband plasmon in the undoped limit, based on Eq. (29). On the Fermi scale, it is not obvious that there is an interband plasmon, although the interacting polarization function develops a smeared resonance around the perturbative
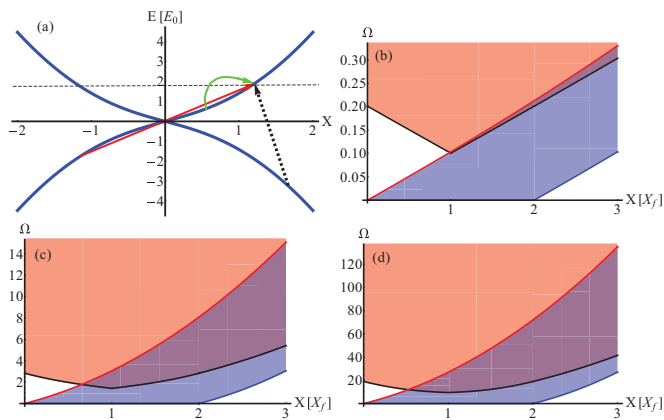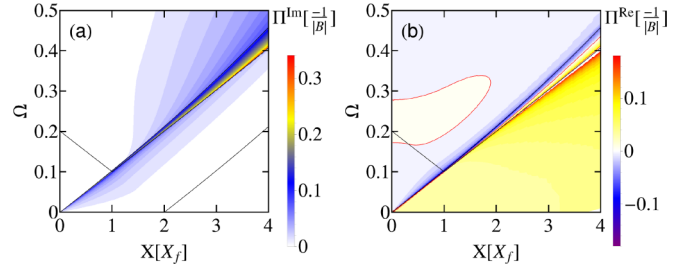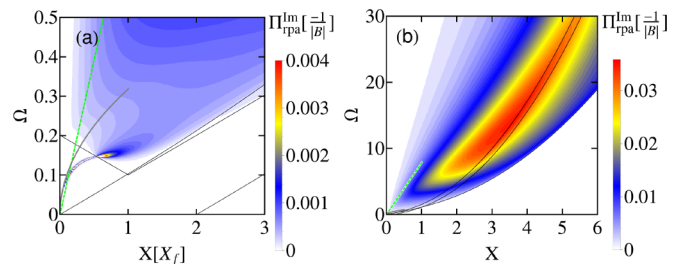


FIG. 12. (Color online) (a) Band structure of the BHZ model with indicated intraband (interband) transitions, green arrow (red and black, dashed arrow), and finite chemical potential. (b)–(d) Boundaries of the spectrum for $X_f \in \{0.1, 1, 3\}$. Interband spectrum in red, intraband spectrum in blue, and mixed area in purple.



FIG. 14. (Color online) $\Pi_{rpa}^{Im}$ for $X_f = 0.1$ with $\alpha = 10$ on the $k_f$ scale (a) and the $q_0$ scale (b). We add an artificial damping in the regions of $\Pi^{Im} = 0$ to make the plasmons visible.
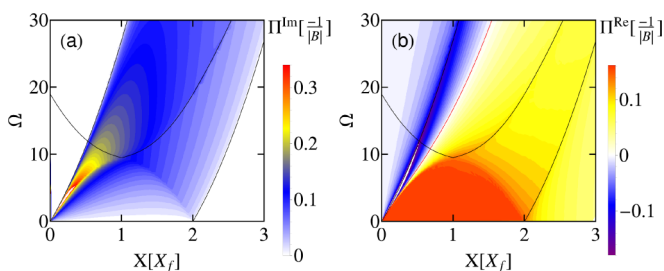
FIG. 15. (Color online) The imaginary (a) and real part (b) of the polarization function for $X_f = 3$. The red line indicates $\Pi^{Re} = 0$.

interband plasmon dispersion for high momenta. Switching to the intrinsic scale, Fig. 14(b), one finds the interband plasmon, corresponding to the single peak in $-\Pi_{rpa}^{Im}$, unperturbed by doping for momenta much larger than $k_f$. The dispersion is the same as for a plasmon in the undoped limit [9]. The two black lines near the peak are just the boundaries of the intraband excitation spectrum, which does not play a role here.

As in the limit of $X \to 0$ the interband plasmon dispersion scales linearly with $\alpha$, $\Omega_p \propto \alpha$, see Eq. (29), while the intraband plasmon frequency is proportional to $\sqrt{\alpha}$; lowering the interaction strength will lead to an overlap of the two resonances below some critical $\alpha$.

(b) *Strong doping of $X_f = 3$.* Strong doping of the system significantly increases the spectral weight, as shown in Fig. 2(b), with the increase of intraband excitations, while most of the interband excitations are Fermi-blocked, leading therefore to an effective decoupling of the two bands. We expect the overall spectrum to be governed by intraband excitations and to resemble the spectrum of a 2DEG, as the Fermi surface lies in the (almost) quadratic part of the spectrum.

The corresponding $\Pi^R$ is plotted in Fig. 15. The single-particle spectrum in panel (a) is peaked at small momenta and at energies close to the upper bound of the intraband spectrum.

The interband part of the spectrum leads only to minor deviations from the 2DEG case [compare with Fig. 10(a)]. The real part of $-\Pi^R$ in panel (b) is strongly negative at the upper boundary of the intraband spectrum, indicating that only a single intraband plasmon will dominate the interacting spectrum. We additionally note that the static limit property for which the polarization is a constant $\tilde{\Pi}(X) = 1$ for $X < 2X_F$, discussed in Sec. IV A, extends also to an area of finite $\Omega$.

The interacting spectrum is shown in Fig. 16 by plotting $\Pi_{rpa}^{Im}$ for the interaction strength $\alpha = 10$. Even for this large Coulomb interaction, we only find the intraband plasmon. This is as expected due to the combined effects of Fermi blocking of interband excitations and increased spectral weight for intraband transitions. The interband plasmon lies in the large overlap of inter- and intraband spectrum, cf. Fig. 14(b), and it is therefore heavily damped and not visible in the overall spectrum.

(c) *Intermediate doping of $X_f = 1$.* For intermediate doping levels like $X_f = 1$, a mixture of Dirac and 2DEG behavior is expected, due to the similar importance of inter- and intraband excitations.

We plot the polarization function $\Pi^R$ in Fig. 17. Indeed, the single-particle spectrum in panel (a) looks like a combination
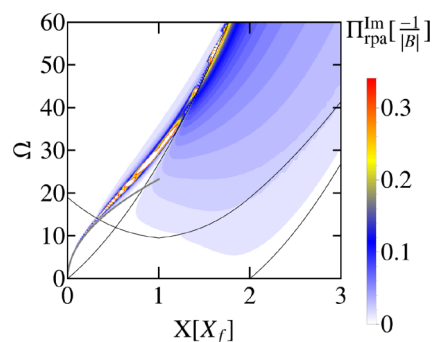


FIG. 16. (Color online) $\Pi_{rpa}^{Im}$ for $X_f = 3$ and $\alpha = 10$. We add an artificial damping in the regions of $\Pi^{Im} = 0$ to make the plasmons visible.

of Figs. 13(a) and 15(a). While the the shape of the polarization resembles the one of the 2DEG, the interband spectrum is now more pronounced and even dominating for $X > 2X_f$. Therefore we could expect both kinds of excitations giving rise to a plasmon mode. The real part of $-\Pi^R$ in panel (b) shows again just a single minimum, following the upper boundary of the intraband spectrum. The deviations from the constant behavior $\tilde{\Pi}(X) = 1$ for $X < 2X_F$ in the case of intermediate doping, see Sec. IV A, are also found for finite $\Omega$.

The interacting spectrum is shown in Fig. 18 by plotting $\Pi_{rpa}^{Im}$ for an interaction strength $\alpha = 10$. It is dominated by a single resonance, lying above the intraband part of the single-particle spectrum. For small momenta, this resonance corresponds to the intraband plasmon. Yet for intermediate momenta, a comparison with the interband plasmon dispersion in Fig. 14(b) indicates that also the interband plasmon contributes to the resonance. A clear distinction between the two is then not possible anymore.

In summary, doping the system offers the possibility to change the excitations spectrum on the Fermi scale from a Dirac to a 2DEG type. The interacting excitation spectrum is usually governed by a single intraband plasmon, while the interband plasmon is hidden in the single-particle background. Only large interaction strengths offer a possibility to see both plasmons in the spectrum. In the following, we will now analyze the influence of both broken p-h symmetry and finite masses, which both offer a way to separate the two plasmons and make them visible in the total spectrum.
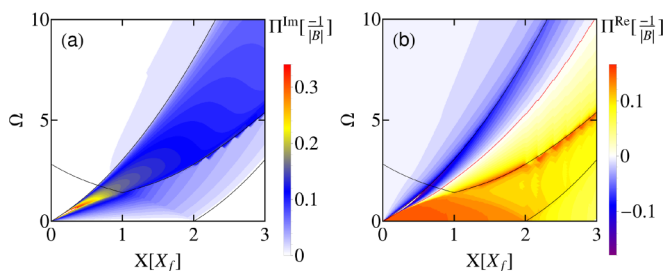


FIG. 17. (Color online) Imaginary (a) and real part (b) of the polarization function for $X_f = 1$. The red line indicates $\Pi^{Re} = 0$.
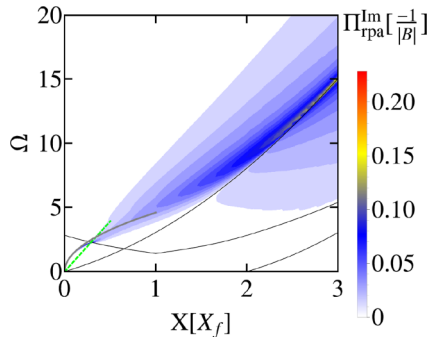
FIG. 18. (Color online) $\Pi_{rpa}^{Im}$ for $X_f = 1$ with $\alpha = 10$. We add an artificial damping in the regions of $\Pi^{Im} = 0$ to make the plasmons visible.

### E. Hg(Cd)Te quantum wells: BHZ model with finite $\xi_D$

A broken particle-hole symmetry, $\xi_D \neq 0$, with small or vanishing mass is the experimental relevant case for HgTe QWs. It also offers the possibility of blocking the interband SPE spectrum close to the minimal excitation energy $\Omega_{min}^{inter}$, resulting in less damped interband plasmons [9].

#### 1. Spectrum

Here, we want to use a similar effect for the intraband excitations in order to separate the inter- and intraband spectrum as well as the two plasmon modes. The broken p-h symmetry introduces an inflection point into the spectrum, $\frac{\partial^2}{\partial X^2}\epsilon_{X,\lambda} = 0|_{X=X_{inf}}$, with momentum $X_{inf}$ and energy $\Omega_{inf}$. For $\xi_D < 0$, it lies in the hole part [$\lambda = -1$] of the spectrum. With a sufficiently small Fermi momentum, $X_f \lesssim X_{int}$, the highest energy intraband excitations involve the Dirac point for momenta on the order of the Fermi momentum; see Fig. 19. The same is true for the lowest energy interband excitations. Due to the vanishing density of states at the Dirac point, both kinds of excitations are suppressed, and therefore inter- and intraband SPE spectrum are effectively separated in energy and momentum. This situation is shown in Fig. 20(a) and Figs. 21(c)–21(e), where the imaginary part of the polarization goes to zero between inter- and intraband parts of the spectrum, fully separating them. There, we choose $X_f = \frac{1}{2}X_{inf}$, $\xi_D = -0.5$, and $\xi_M = 0$. This blocking effect holds for small momenta up to roughly $2X_{inf}$, indicated by the
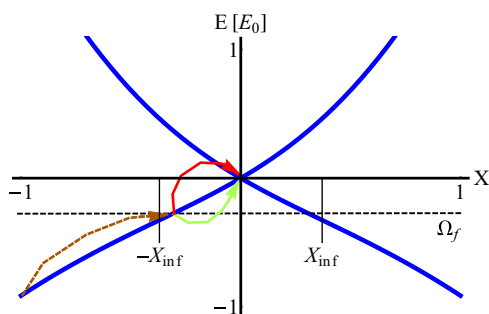


FIG. 19. (Color online) Band structure for $\xi_D = -0.5$. Both low-energy interband excitations (red arrow) and high-energy intraband excitations (green arrow) involve the Dirac point.
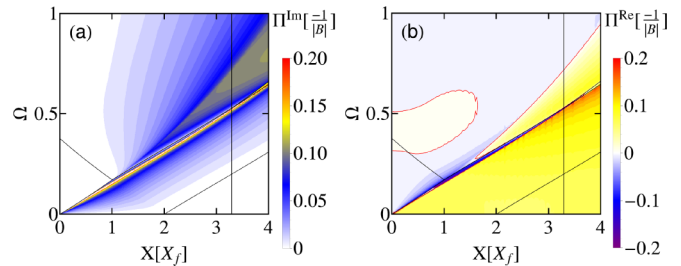


FIG. 20. (Color online) $\Pi^{Im}$ (a) and $\Pi^{Re}$ (b) for $X_f = \frac{1}{2}X_{inf} = 0.185$ and $\xi_D = -0.5$. The red line indicates $\Pi^{Re} = 0$.

black vertical line in Fig. 20 at $X \approx 3.2$. For larger momenta the high-energy intraband excitation go from deep in the valence band directly to the Fermi surface—the blocking effect of the Dirac point is gone; see dashed arrow in Fig. 19.

In Fig. 20(b), $\Pi^{Re}$ shows one major difference in comparison to the p-h symmetric case of weak doping in Fig. 13(b). At the border of intra- and interband spectrum a strong antiscreening region is formed. For sufficiently low $\alpha$ a plasmon should exist there, clearly separated from the second antiscreening region at higher $\Omega$, giving rise to the possibility of observing both intra- and interband plasmons. This can be seen in Fig. 21, where we plot $\Pi_{rpa}^{Im}$ for $\alpha = 2$ (a)
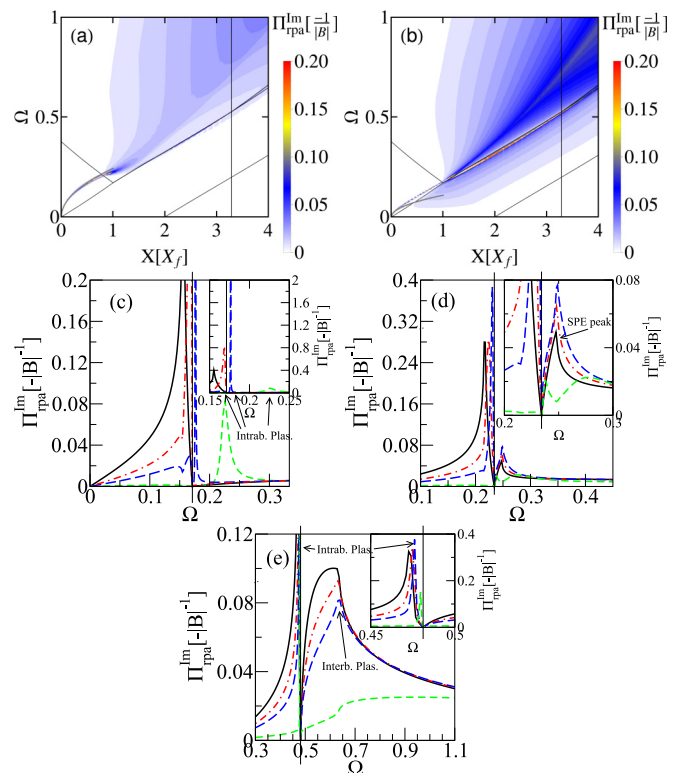


FIG. 21. (Color online) Interacting polarization function $\Pi_{rpa}^{Im}$ for $X_f = \frac{1}{2}X_{inf} = 0.185$, $\xi_D = -0.5$, $\xi_M = 0$, and $\alpha = 2$ (a) and $\alpha = 0.4$ (b). (c)–(e) show line cuts for fixed $X = X_f$, $X = 1.4X_f$, and $X = 3X_f$, respectively, with $\alpha \in \{0, 0.2, 0.4, 2\}$ in black solid line, red dot-dashed line, blue long-dashed line, and green short-dashed line, respectively. The black, vertical line separates the inter- and intraband SPE region.

and $\alpha = 0.4$ (b). Panels (c)–(e) show line cuts for fixed momenta $X \in \{1, 1.4, 3\} X_f$ and different interaction strengths $\alpha \in \{0, 0.2, 0.4, 2\}$.

For large interaction strength $\alpha = 2$, the intraband plasmon decays into the interband SPE spectrum; see panel (a) for $X \approx X_f$ and the green short dashed line in panel (c). Most of the spectral weight stays there also for larger momenta, as $\Pi_{rpa}^{Im}$ is close to 0 in the intraband SPE region and the resonance between inter- and intraband SPE spectrum is weak. The latter can be best seen in the insets of panels (d) and (e), represented by the green short dashed line peaked slightly above [panel (d)] or below [panel (e)] the black vertical line separating intra- and interband SPE region. Yet even with the peak being small, it indicates the formation of a slightly damped plasmon, but with small spectral weight. The missing spectral weight is transferred to higher energies into the interband SPE region. For intermediate momenta, a second plasmon branch forms; see panel (a) for $X_f < X < 2X_f$ and the second peak of the green short-dashed line in the inset of panel (d). For even higher momenta, $X > 2X_f$, it overlaps with the forming interband plasmon leading to a broad charge resonance without clear peak; see green short-dashed line in panel (e) for $\Omega > 0.7$.

The picture changes for smaller interaction strength. For $\alpha = 0.4$, the intraband plasmon decays in the region between inter- and intraband SPE spectrum, indicated by the strong peak of the blue long-dashed line in panel (c). As the single-particle excitations in this region are suppressed due to the Dirac point, the plasmon leads to a high and narrow peak of $\Pi_{rpa}^{Im}$. Considering larger momenta $X > X_f$, the resonance is split: one part forms an intraband plasmon in the intraband SPE region; see blue long-dashed line peaked slightly below the black vertical line in panels (d) and (e). The second part stays in the interband SPE region, where it enhances the SPE peak [black line in the inset of panel (d)] for intermediate momenta $X_f < X < 2X_f$. For momenta $X \gtrsim 2X_f$, an interband plasmon forms, as shown in panel (e). There, the broad single-particle peak (black line) around $\Omega = 0.6$ gets reshaped into a clear peaked resonance (blue long-dashed line)—the interband plasmon.

### 2. Experimental parameters

Taking the experimental parameters from Sec. II F, $q_0 \approx 0.4 \frac{1}{nm}$ and $E_0 \approx 140$ meV, one finds for the plots in Fig. 21 the Fermi momentum $k_f \approx 0.07 \frac{1}{nm}$ and chemical potential $\mu \approx -24$ meV $= -\hbar \times 36$ THz. The plot range is therefore $q \in [0, 0.74]q_0 = [0, 0.3]\frac{1}{nm}$ and $\omega \in [0,1]\frac{E_0}{\hbar} = [0, 210]$ THz and thus of the right order of magnitude for experimental techniques like Raman spectroscopy or electron-loss spectroscopy.

### 3. Spectral weight and the f-sum rule

Both plasmonic resonances in Fig. 21(b) overlap for $X \approx X_f$, before they separate for higher momenta. Therefore the question arises whether one can really speak of a clear distinction between inter- and intraband plasmons for larger momenta. Here, we want to study the $f$-sum rule and thus the spectral weight of the different excitations.
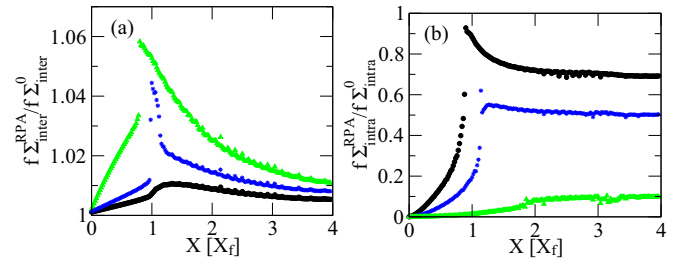


FIG. 22. (Color online) (a) The ratio $\frac{f \sum_{inter}^{RPA}}{f \sum_{inter}^{0}}$ of interacting over noninteracting $f$-sum rule of the interband excitations. Black dots are for $\alpha = 0.2$, blue stars stand for $\alpha = 0.4$, and green triangles for $\alpha = 2$. (b) The same for the ratio $\frac{f \sum_{intra}^{RPA}}{f \sum_{intra}^{0}}$ of the intraband excitations. For all plots: $X_{max} = 4X_f$ and $\beta = 4$.

The relative deviations of numerical to analytical $f$-sum rule are again of the order $10^{-3}$ and thus negligible. Figure 22(a) shows the ratio of spectral weight in the interband SPE region for the interacting over the noninteracting case, $\frac{f \sum_{inter}^{RPA}}{f \sum_{inter}^{0}}$, and panel (b) the same for the intraband SPE region. The intraband plasmon lying between these two regions for $X < X_f$ is excluded. As for cutoffs $\beta > 1$ one usually has $f \sum_{inter}^{0} \gg f \sum_{intra}^{0}$, transfer of spectral weight from one region to the other can lead to quantitatively different relative changes of spectral weight in panels (a) and (b). As a key result, we find that there is always spectral weight missing in the intraband SPE region. For small momenta, $X < X_f$, the weight goes into the undamped intraband plasmon (this follows directly from the conservation of the $f$-sum rule for interacting and noninteracting systems), while at larger momenta it is transferred to higher energies into the interband SPE region. Yet, the increase is only about 2% at $X \gtrsim 2X_f$, such that we can conclude that the plasmon between the inter- and intraband SPE region is a pure intraband plasmon with a reduced spectral weight. The plasmon in the interband region is the interband plasmon we know already from the undoped system, see Fig. 6, with a slight increased spectral weight from the intraband SPE region.

### 4. Small gap $\xi_M \neq 0$

Deviations in the thickness of a Hg(Cd)Te QW lead to the opening of a small gap in the band structure, resulting in a topological trivial $\xi_M > 0$ or nontrivial $\xi_M < 0$ system. Apart from the possible appearance of edge states, which is beyond the scope of this paper, a small mass works in opposition to the blocking effect of finite $\xi_D$, as it generates a finite density of states for $X = 0$. In the following, we therefore show that the blocking effect of a finite $\xi_D$ is robust against the opening of small gaps.

In Fig. 23 we plot the noninteracting and interacting spectrum for $\xi_D = -0.5$ and a small mass $\xi_M = 0.01 \approx 1.4 \frac{meV}{E_0}$. A comparison with Figs. 20 and 21 shows that the small mass has just the effect of separating the inter- and intraband SPE region additionally. Thus we conclude that the idea of observing both plasmons in experiments is robust against slight deviations in the mass and therefore the thickness of the Hg(Cd)Te QW.
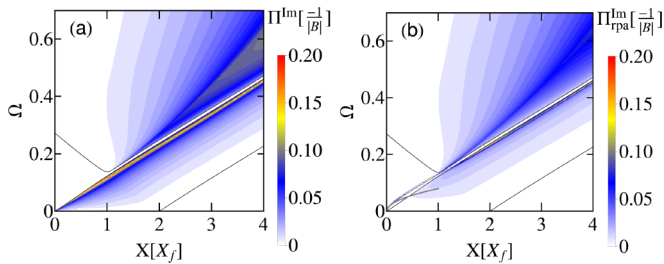
FIG. 23. (Color online) The imaginary part of the noninteracting polarization $\Pi^{Im}$ (a) and the interacting one $\Pi^{Im}_{rpa}$ (b) with $\alpha = 0.4$. $X_f = 0.133 < \frac{1}{2}X_{\inf}$, $\xi_M = 0.01$, and $\xi_D = -0.5$.

### F. Topology: BHZ model with large $\xi_M \neq 0$

A finite Dirac mass opens a gap in the band structure and changes the pseudospin, and therefore the overlap factor, in a nontrivial fashion. Thus we can expect in general a quite different behavior for positive and negative mass. Yet, for these differences to occur on the intrinsic scale and thus influence the interband plasmons, $|\xi_M|$ should be of the order of 1. In the following, we study such large masses, both negative and positive, with p-h symmetry. While not experimentally relevant for HgTe QWs, it offers the possibility to study the effect of a topological band structure on the electronic excitations, including plasmons. We also note here that the dispersion of the BHZ model becomes purely parabolic for the mass $\xi_M = -\frac{1}{4}$: $\epsilon_{X,\lambda} = \frac{\lambda}{4} + X^2(\lambda - \xi_D)$. In this limit, the polarization function, Eq. (5), can be calculated analytically.

#### 1. Large, negative mass

For the parameters $X_f = 0.33$ and $\xi_M = -\frac{4}{9}$ we plot the polarization $\Pi^R$ in Figs. 24(a) and 24(b). The mass separates intra- and interband SPE regions for $X \lesssim 2X_f$. Compared to the massless cases of $X_f = 0.1$, Fig. 13, and $X_f = 1$, Fig. 17, the interband SPE spectrum is enhanced due to the combination of enhanced overlap factor and low doping, thus
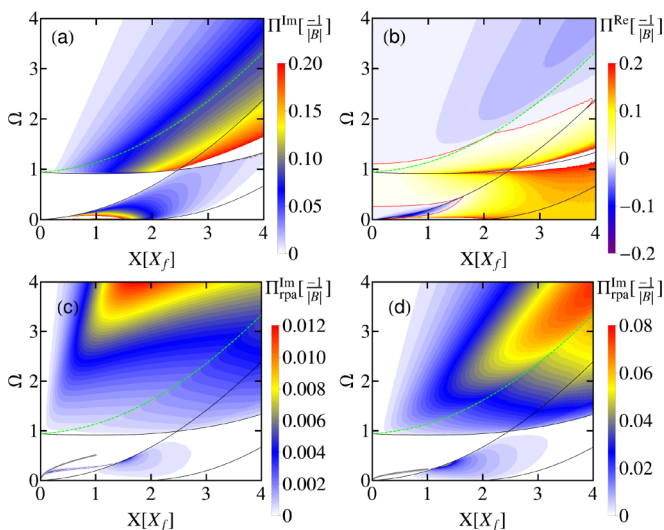


FIG. 24. (Color online) (a) Imaginary and (b) real part of the polarization $\Pi^R$. (c) and (d) show $\Pi^{Im}_{rpa}$ with $\alpha = 10$ and $\alpha = 2$, respectively. $\xi_M = -\frac{4}{9}$ and $X_f = 0.33$ in all plots.
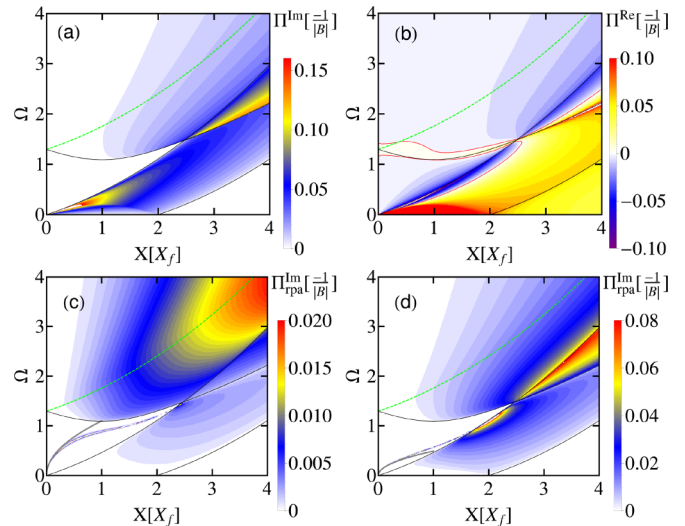


FIG. 25. (Color online) (a) Imaginary and (b) real part of the polarization $\Pi^R$. (c) and (d) show $\Pi^{Im}_{rpa}$ with $\alpha = 10$ and $\alpha = 2$, respectively. $\xi_M = \frac{4}{9}$ and $X_f = 0.33$ in all plots.

small Fermi blockade. Due to the flat band structure, even for $X_f = 0.33$ the chemical potential is just barely above the gap. An interesting consequence of this strong interband transition can be seen in panel (b), where we find two distinct areas where $-\Pi^{Re}$ becomes negative. As a consequence, inter- and intraband plasmons will always be separated, with the intraband plasmon being confined to low energies. This stems from the fact that the electrons in the conduction band are pseudospin polarized, such that intraband excitations to much higher momenta and energies, where the pseudospin shows in the opposite direction, are not possible.

This is confirmed in panels (c) and (d), where we plot $\Pi^{Im}_{rpa}$ with $\alpha = 10$ and $\alpha = 2$, respectively. All the spectral weight of the intraband SPE region goes into the plasmon, which at least for $\alpha = 2$ follows very well the $\sqrt{X}$ law. The interband spectrum is dominated by the interband plasmon, having of course a much broader peak due to damping (finite Im[$\Pi^R$]).

The dashed, green line in the interband spectrum in Fig. 24 indicates the energy at which excitation processes going from momentum $X + X_f$ to $X_f$ with $X \| X_f$ are possible; see black, dashed arrow in Fig. 12(a). Usually suppressed by the overlap factor, a large negative mass enhances these excitations by increasing the overlap of the bands to near unity for small Fermi momenta. Figures 24(b) and 24(d) show that the interband plasmons mainly occur above this line, indicating that the described excitation process is important for the collective excitation. As the process is forbidden by helicity in the pure Dirac system, it is one reason why the BHZ model supports intrinsic plasmons while the Dirac model does not.

#### 2. Large, positive mass

For the parameters $X_f = 0.33$ and $\xi_M = \frac{4}{9}$ we plot the polarization in Figs. 25(a) and 25(b). Compared to the negative mass case, the interband spectrum is much weaker. This is a result of the lower overlap factor and the higher chemical potential (the band structure is not as flat as in the TI phase), leading to a stronger Fermi blockade. For the real part of the

polarization, this has the effect that the two former distinct areas of sign reversal now almost merge. The interband excitations are so weak that the minimum $-\Pi^{Re}$ always lies closely above the intraband SPE region, indicating that it is the main source for plasmons.

In panel (c) for $\alpha = 10$, one can identify both inter- and intraband plasmon. Interestingly, the polarization is clearly higher in the pure interband SPE region than in the mixed inter- and intraband SPE spectrum, suggesting that the latter serves as an additional damping for the interband plasmon. Going to the smaller interaction strength $\alpha = 2$ in panel (d), one finds just a single resonance following the upper boundary of the intraband SPE spectrum. Thus we conclude that the interacting spectrum for moderate interaction strength is governed by just intraband plasmons. The interband excitations are too weak to support an additional plasmon but for very high interactions— a consequence of the effective decoupling of the bands by the overlap factor.

## V. CONCLUSION

We have analyzed the dynamical and static polarization properties in the random phase approximation of Hg(Cd)Te quantum wells described by the Bernevig-Hughes-Zhang (BHZ) model. In the static undoped limit, due to the presence of quadratic terms in the BHZ model and hence to the natural length scale $B/A$, the induced charge density in response to a test charge has a finite spatial extent. This is in contrast to the pointlike screening charge obtained with the continuous Dirac model of graphene. In the doped regime, we have observed Friedel oscillations with an intermediate decay behavior between the Dirac ($r^{-3}$) and the 2DEG ($r^{-2}$) cases.

The discussion of the full dynamical polarization function has been focused on the appearance of new interband plasmons due to the interplay of Dirac and Schrödinger physics. In principle, we expect these plasmons to appear in multiband systems where the imaginary part of the polarization function decays faster with energy than the one in the Dirac case

($\omega^{-1}$), which is the case for the BHZ model (decay as $\omega^{-2}$). These plasmons appear already in the undoped system at experimentally relevant parameters, but it is also possible to observe them in the doped regime, where they coexist with the usual intraband plasmons. This is favored by broken particle-hole symmetry in the BHZ model, which allows for the presence of both a Dirac point and an inflection point in the band structure. The behavior of these two collective modes is also influenced by the topology of the band structure. Indeed the two plasmons tend to merge into one another in a gapped trivial insulator, while they remain distinct resonances in the topological insulator phase. We have shown that these new plasmons should appear for momenta and energies on the right order of magnitude for experimental techniques like Raman spectroscopy or electron-loss spectroscopy on Hg(Cd)Te quantum wells.

The wide range of parameters considered in this paper, including the regime of topologically trivial and nontrivial insulators, should make our results applicable to all kinds of materials described by phenomenological models interpolating between Dirac and Schrödinger fermion physics.

Throughout this article, we have only discussed bulk excitations of this peculiar two-dimensional system. Hence, we have totally ignored the influence of edge states in the topologically nontrivial regime of the model in the presence of physical boundaries.

An extension of our analysis to finite-size systems might yield exciting new physics, where we expect an interplay of one-dimensional and two-dimensional collective charge excitations.

[1] M. Z. Hasan and C. L. Kane, Rev. Mod. Phys. **82**, 3045 (2010).

[2] X.-L. Qi and S.-C. Zhang, Rev. Mod. Phys. **83**, 1057 (2011).

[3] J. C. Budich and B. Trauzettel, Phys. Status Solidi RRL **7**, 109 (2013).

[4] M. König, S. Wiedmann, C. Brüne, A. Roth, H. Buhmann, L. W. Molenkamp, X.-L. Qi, and S.-C. Zhang, Science **318**, 766 (2007).

[5] D. Hsieh, D. Qian, L. Wray, Y. Xia, Y. S. Hor, R. J. Cava, and M. Z. Hasan, Nature (London) **452**, 970 (2008).

[6] C. Xu and J. E. Moore, Phys. Rev. B **73**, 045322 (2006).

[7] C. Wu, B. A. Bernevig, and S.-C. Zhang, Phys. Rev. Lett. **96**, 106401 (2006).

[8] B. A. Bernevig, T. L. Hughes, and S.-C. Zhang, Science **314**, 1757 (2006).

[9] S. Juergens, P. Michetti, and B. Trauzettel, Phys. Rev. Lett. **112**, 076804 (2014).

[10] B. Wunsch, T. Stauber, F. Sols, and F. Guinea, New J. Phys. **8**, 318 (2006).

[11] E. H. Hwang and S. Das Sarma, Phys. Rev. B **75**, 205418 (2007).

[12] V. N. Kotov, B. Uchoa, V. M. Pereira, F. Guinea, and A. H. Castro Neto, Rev. Mod. Phys. **84**, 1067 (2012).

[13] E. Barnes, E. H. Hwang, R. E. Throckmorton, and S. Das Sarma, Phys. Rev. B **89**, 235431 (2014).

[14] J. Hofmann, E. Barnes, and S. Das Sarma, arXiv:1405.7036.

[15] T. Stauber, J. Phys.: Condens. Matter **26**, 123201 (2014).

[16] T. Low, R. Roldán, W. Han, F. Xia, P. Avouris, L. M. Moreno, and F. Guinea, arXiv:1404.4035.

[17] A. Scholz, T. Stauber, and J. Schliemann, Phys. Rev. B **88**, 035135 (2013).

[18] P. Michetti, J. C. Budich, E. G. Novik, and P. Recher, Phys. Rev. B **85**, 125309 (2012).

[19] V. N. Kotov, B. Uchoa, V. M. Pereira, F. Guinea, and A. H. Castro Neto, Rev. Mod. Phys. **84**, 1067 (2012).

[20] A. N. Grigorenko, M. Polini, and K. S. Novoselov, Nat. Photon. **6**, 749 (2012).

[21] B. Büttner, C. X. Liu, G. Tkachov, E. G. Novik, C. Brüne, H. Buhmann, E. M. Hankiewicz, P. Recher, B. Trauzettel, S. C. Zhang, and L. W. Molenkamp, Nat. Phys. **7**, 418 (2011).

[22] M. J. Schmidt, E. G. Novik, M. Kindermann, and B. Trauzettel, Phys. Rev. B **79**, 241306 (2009).

[23] A. L. Fetter and J. D. Walecka, *Quantum Theory of Many-Particle Systems* (McGraw-Hill, New York, 1971).

[24] P. Di Pietro, M. Ortolani, O. Limaj, A. Di Gaspare, V. Giliberti, F. Giorgianni, M. Brahlek, N. Bansal, N. Koirala, S. Oh, P. Calvani, and S. Lupi, Nat. Nano. **8**, 556 (2013).

[25] P. Nozieres and D. Pines, *The Theory of Quantum Liquids* (Perseus Books, New York, 1966).

[26] J. Sabio, J. Nilsson, and A. H. Castro Neto, Phys. Rev. B **78**, 075410 (2008).

[27] V. N. Kotov, V. M. Pereira, and B. Uchoa, Phys. Rev. B **78**, 075433 (2008).

[28] P. K. Pyatkovskiy, J. Phys.: Condens. Matter **21**, 025506 (2009).

[29] G. Giuliani and G. Vignale, *Quantum Theory of the Electron Liquid* (Cambridge University Press, Cambridge, 2008).

[30] T. Ando, J. Phys. Soc. Jpn. **75**, 074716 (2006).

[31] E. V. Gorbar, V. P. Gusynin, V. A. Miransky, and I. A. Shovkovy, Phys Rev. B **66**, 045108 (2002).

[32] M. J. Lighthill, *Introduction to Fourier Analysis and Generalized Functions* (Cambridge University Press, Cambridge, 1958).

[33] S. M. Badalyan, A. Matos-Abiague, G. Vignale, and J. Fabian, Phys. Rev. B **81**, 205314 (2010).

[34] Due to the details of the derivation of the analytical expansion in Eq. (22), the same is not possible for the limit $B \rightarrow 0$, as there the defined cutoff $\Lambda = \lambda \frac{|B|}{A^2}$ would go to zero.